

tektonika



Kinematic Evolution of the Tangra Yumco Rift, South-Central Tibet

Aislin N. Reynolds (1) *1, Andrew K. Laskowski (10), Caden J. Howlett (10), Devon A. Orme (10), Kurt E. Sundell (10), Michael H. Taylor⁴, Adam M. Forte (10), Spencer Dixon¹, Fulong Cai (10), Xudong Guo (10), 7, Lin Ding 1006

¹Department of Earth Sciences, Montana State University, Bozeman, MT, USA | ²Now at Department of Geosciences, University of Arizona, Tucson, AZ, USA | ³Department of Geosciences, Idaho State University, Pocatello, ID, USA | ⁴Department of Geology, University of Kansas, Lawrence, KS, USA | ⁵Department of Geology & Geophysics, Louisiana State University, Baton Rouge, LA, USA | ⁶Institute of Tibetan Plateau Research, Chinese Academy of Sciences, Beijing, China | Now at National Disaster Reduction Center of China (NDRCC), Beijing, China

We investigate rifting during continental collision in southern Tibet by testing kinematic models for two classes of rifts: Tibetan rifts are defined as >150 km in length and crosscut the Lhasa Terrane, and Gangdese rifts are <150 km long and isolated within the high topography of the Gangdese Range. Discerning rift kinematics is a crucial step towards understanding rift behavior and evolution that has been historically limited. We evaluate spatiotemporal trends in fault displacement and extension onset in the Tangra Yumco (TYC) rift and several nearby Gangdese rifts and examine how contraction and rift exhumation relate to evolution of the Gangdese drainage divide. Igneous U-Pb and zircon (U-Th)/He (ZHe) results indicate rift footwall crystallization between ~59-49 Ma and cooling between ~60-4 Ma, respectively, with ZHe ages correlating with sample latitude. Samples from Gangdese latitudes (~29.4-29.8°N) yield predominantly Oligocene-early Miocene ages, whereas samples north of ~29.8°N yield both late Miocene-Pliocene ages and Paleocene-Eocene ages. Thermal history models indicate two-stage cooling, with initially slow cooling followed by accelerated cooling during late Miocene-Pliocene time. From spatial distributions of ZHe ages we interpret: (1) \sim 28-16 Ma ages from Gangdese latitudes reflect exhumation along contractional structures, (2) \sim 8-4 Ma ages reflect rift-related exhumation, and (3) \sim 60-48 Ma ages indicate these samples experienced lesser rift exhumation. Our data are consistent with a segment linkage evolution model for the TYC rift, with interactions between rifts and contractional structures likely influencing the evolution of topography and location of the Gangdese drainage divide since Miocene time.

Robin Lacassin Associate Editor: **Dave Whipp Mohamed Gouiza**

Anne Replumaz Konstanze Stübner **Reinhard Wolff**

> 14 March 2023 Accepted: 11 March 2024 Published: 8 July 2024

Plain Language Summary Tibet is a unique location where we can study the complex interactions between continental collision and stretching of the Earth's crust. The linear structures and valleys that form due to crustal extension and normal faulting are called rifts. The study of rifts is important because the rocks they expose can record thermal changes due to movement of the Earth's crust that are otherwise inaccessible to study. Additionally, rift behavior can be related to large-scale processes like shifts in tectonic plates, which make up the rigid outer shell of the Earth, that occur over long timescales and can be difficult to observe. Rifts also interact with topography, influence river systems, and can cause changes in rainfall distribution across a landscape by forming drainage divides. Despite their importance, the processes that occur during rift formation and evolution are not well understood.

In this study we use field and radiometric dating techniques to investigate what the shape, orientation, and timing of activity along the Tangra Yumco rift can tell us about rift behavior. look at the spatial distributions of cooling ages to investigate changes over time and better understand rift behavior in south-central Tibet. Our results suggest Tibetan rifts form through the linkage of smaller normal fault segments into larger and longer structures over time, with their evolution likely related to continued collision between India and Asia. Interactions between rifts and contractional structures have likely influenced the evolution of topography and drainage patterns in southern Tibet since at least sixteen million years ago.

^{*⊠} geoaislin@gmail.com

Introduction 1

Mountain belts and continental plateaus that owe their high elevations to crustal shortening frequently undergo extension coeval with plate convergence (Burchfiel and Royden, 1985). Synconvergent extension has been documented in orogenic belts around the world, including the Himalayan-Tibetan orogenic system (Figure 1 Burchfiel and Royden, 1985; Burchfiel et al., 1992; England and Houseman, 1989; McCaffrey and Nabelek, 1998; Kapp and Guynn, 2004) the North American Cordillera (Wells and Hoisch, 2008; Wells et al., 2012; Long et al., 2015; Platt and England, 1994), and the Andes (Allmendinger, 1986; Kay and Mahlburg Kay, 1993; Marrett and Strecker, 2000; Giovanni et al., 2010; Hughes et al., 2019). Despite this widespread recognition, uncertainties remain in our understanding of rifting during plate convergence: the conditions under which rifts initiate, normal fault growth and evolution patterns, and the influence of deep versus shallow crustal processes are several critical questions that are unresolved (e.g., Wells et al., 2012; Huntington and Klepeis, 2018; Brune et al., 2023).

Innovation and advancements in geoand thermochronology techniques create new opportunities to develop spatially robust datasets that facilitate investigation of uncertainties in rift behavior through testing of kinematic models (e.g., Curry et al., 2016). We consider two classes of rifts in Tibet: (1) Tibetan rifts, which we define as rifts that are >150 km in length and crosscut the Lhasa Terrane, and (2) Gangdese rifts, which we define as rifts generally <150 km in length that are isolated within the high topography of the Gangdese Range of southern Tibet (Figure 2 Yin, 2000; Burke et al., 2021). Both of these classes are located south of the zone of conjugate strike-slip faulting along the Bangong-Nujiang Suture Zone (i.e. the "chord" of Armijo et al., 1986), and north of the Indus-Yarlung suture zone within the Lhasa Terrane. *Yin* (2000) noted a difference in the spatial distributions of these two classes of rifts, with Tibetan rifts spaced \sim 146 \pm 34 km apart and Gangdese rifts spaced \sim 46 \pm 7 km from each other in southern Tibet. Collection of low-temperature thermochronology data and structural observations along strike of the southern TYC rift and three nearby Gangdese rifts allows evaluation of spatial patterns of fault displacement and extension onset to determine a best fit kinematic model for rifting.

We investigate the Tangra Yumco (TYC) rift and nearby Gangdese rifts in south-central Tibet to address the following research questions: (1) when did the TYC rift and Gangdese rifts initiate?; (2) what are the kinematics of the TYC rift and how did TYC evolve through time?; (3) how does TYC compare to other rifts in Tibet?; (4) what can the timing and rates of extension in TYC and Gangdese rifts reveal about interactions between contractional and extensional structures and the regional tectonics of southern Tibet?; and (5) how might rift processes relate to and interact with the Gangdese drainage divide? We investigate these questions and provide a review of the geologic history and prior research related to rifting in southern Tibet. We introduce key hypotheses related to the kinematics of east-west extension in Tibet and development of the Gangdese drainage divide, which separates the internally and externally drained portions of the Tibetan Plateau.

1.1 Rift Kinematics

Characterizing rift kinematics is an essential step towards understanding the geologic and tectonic variables impacting rift initiation and growth and can advance our understanding of the forces which drive continental rifting in contractional settings (e.g., Yin, 2000; Sundell et al., 2013; Curry et al., 2016). Researchers have hypothesized that the orientation, structural style, timing of onset, magnitudes, and rates of extension of rifts in Tibet are spatially variable, with differences in rift evolution and behavior influenced by the following factors: (a) rift position relative to the India-Asia convergence vector (Figure 1; Kapp and Guynn, 2004), (b) variations in the mechanical and/or thermal conditions of the lithosphere (*England and Houseman*, 1989; *Molnar and* Tapponnier, 1978; Molnar et al., 1993; Buck, 1991, 1993; Bischoff and Flesch, 2018), (c) strength contrasts or decoupling between the upper and lower crust (e.g., Copley et al., 2011), (d) the orientation and location of subducting Indian lithosphere (e.g., Yin, 2000; Styron et al., 2015; Klemperer et al., 2022), (e) interactions with pre-existing and coevally formed structures (Taylor et al., 2003; Taylor and Yin, 2009; Ratschbacher et al., 2011; Sundell et al., 2013), or a combination of these and other factors (e.g., Labrousse et al., 2016; Wolff et al., 2019).

A model proposed by Kapp et al. (2008) details Tibetan rift geometry and kinematics based on observations from the Lunggar and Yadong-Gulu rifts (Figure 1; section 2.2.4.) and provides a baseline for comparison and evaluation of TYC rift kinematics. In this model, rifts initiate as graben or half-graben basins bounded by a dominant high-angle normal fault which soles into a sub-horizontal shear zone at depth. As magnitudes of extension increase, tectonic unloading drives isostatic rebound and back-rotation of the footwall, allowing slip at lower angles but favoring slip along progressively younger basin-stepping high-angle faults. Enhanced isostatic rebound driving exhumation in areas of maximum horizontal extension (low-angle) or accommodation zones between overlapping fault segments (high-angle) may form intra-basin topographic highs capable of establishing new drainage divides (Anders and Schlische, 1994; Faulds et al., 1998; Kapp et al., 2008). This model is similar to rolling-hinge models proposed for the North American Cordillera (Buck, 1988; Wemicke, 1992) where high-angle basin-stepping fault segments may progressively link to form larger fault structures and

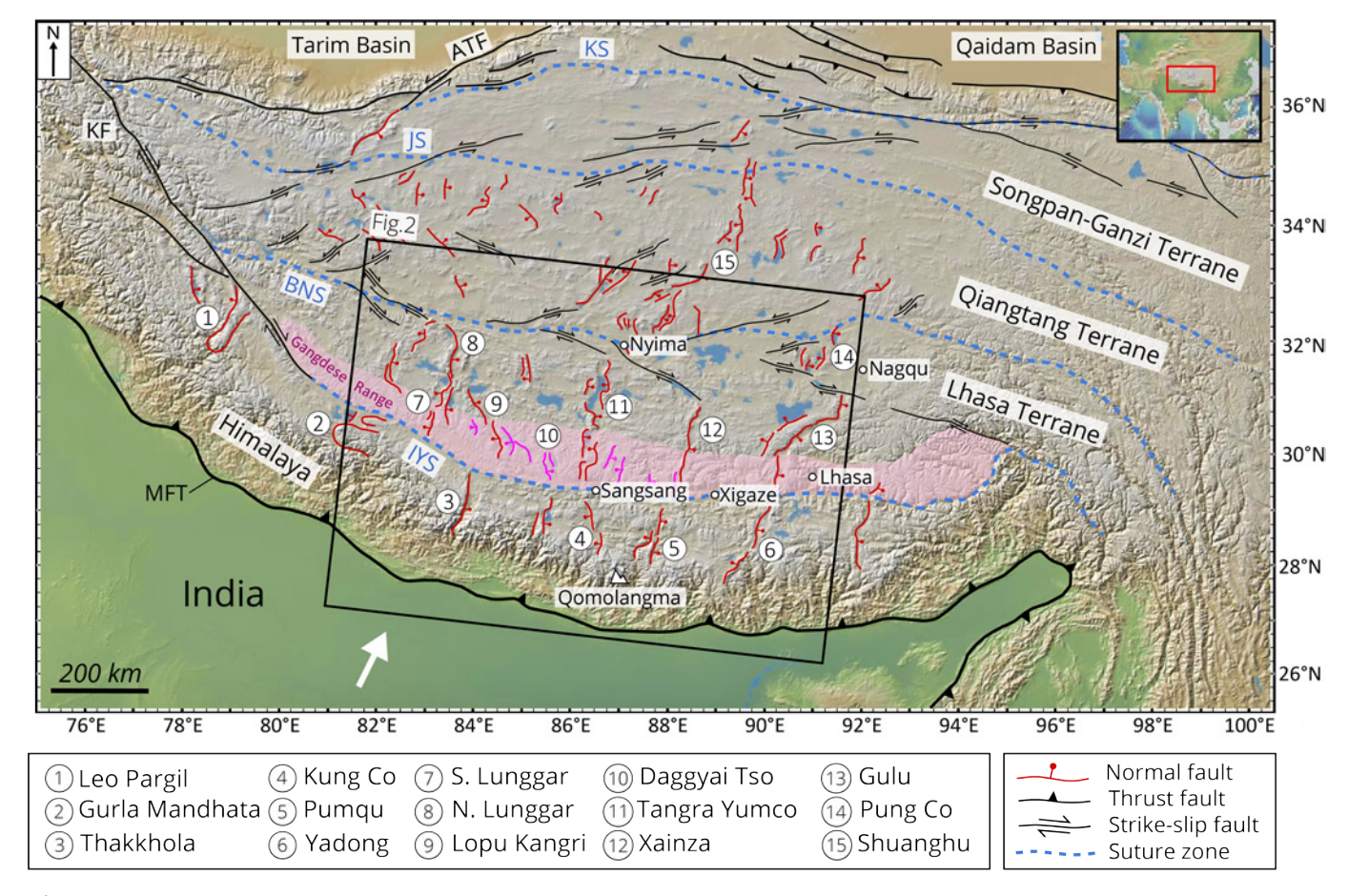


Figure 1 - Digital elevation model of the Tibetan Plateau highlighting major structures and tectonic features adapted from Taylor and Yin (2009) with fault traces from HimaTibet database (Styron et al., 2010). 1 = Leo Pargil (Thiede et al., 2006); 2 = Gurla Mandhata dome (Murphy et al., 2002; McCallister et al., 2014); 3 = Thakkhola graben (Coleman and Hodges, 1995; Garzione et al., 2003); 4 = Kung Co graben (Maheo et al., 2007; Lee et al., 2011); 5 = Pumqu/Dinggye rift (Arma Drime massif; Jessup et al., 2008; Kali et al., 2010); 6 = Yadong rift (Ratschbacher et al., 2011); 7 = South Lunggar rift (Styron et al., 2013); 8 = North Lunggar rift (Kapp et al., 2008; Sundell et al., 2013); 9 = Lopu Kangri rift (Yin and Harrison, 2000; Sanchez et al., 2013; Laskowski et al., 2017); 10 = Daggyai Tso graben (Yin and Harrison, 2000; Williams et al., 2001); 11 = Tangra Yumco rift (Wolff et al., 2019, 2023, and this study); 12 = Xainza rift (Armijo et al., 1986; Hager et al., 2009); 13 = Gulu rift (Harrison et al., 1995; Kapp et al., 2005; Ratschbacher et al., 2011); 14 = Pung Co rift (Kapp et al., 2008); 15 = Shuanghu graben (Blisniuk et al., 2001; Li et al., 2001). White arrow indicates convergence vector of India relative to Asia. Suture zones shown as dashed blue lines. BNS = Bangong- Nujiang suture; IYS = Indus-Yarlung suture; JS = Jinsha suture; KS = Kunlun suture; KF = Karakorum fault; ATF = Altyn Tagh fault; MFT = Main Frontal Thrust. Gangdese rifts shown in pink. Topography from GeoMapApp.

preferentially reorganize to a simpler configuration through time.

We consider four possible models for fault growth and rift evolution: (A) tip propagation, (B) tectonically influenced tip propagation, (C) segment linkage, or (D) constant fault length (Figure 3). models represent a spectrum of fault behavior, with tip propagation and constant fault length representing end member models, and tectonically influenced tip propagation and segment linkage involving some aspect of fault tip propagation in their behavior. Each kinematic model is distinguished by its predictions of specific map patterns of fault displacement and spatial distributions for the timing of extension onset (Figure 3). Assessing along strike trends in thermochronologic data can thus provide valuable information towards predicting how faults accumulate displacement and lengthen through time, furthering our understanding of how natural fault systems evolve (e.g., Curry et al., 2016).

The tip propagation model (A) suggests extension initiation near Central TYC and rift propagation to the north and south through time, predicting a symmetric map pattern of fault displacement and the age of extension onset to be oldest in Central TYC and younger towards the north and south. Tectonically influenced tip propagation (B) predicts an older age of extension onset at one end of the TYC rift (e.g., southern TYC) with rift propagation and progressively younger ages of extension onset focused in one direction (e.g., northward) driven by tectonic controls. Segment linkage (C) suggests rift initiation as individual, segmented normal faults along the TYC rift which propagate and link to form one larger fault system through time, predicting variable magnitudes of extension and a complexity of extension onset timing along strike due to the irregular behavior of individual fault segments. Finally, the constant fault length model (D) suggests TYC initiated at near present-day length (~250 km)

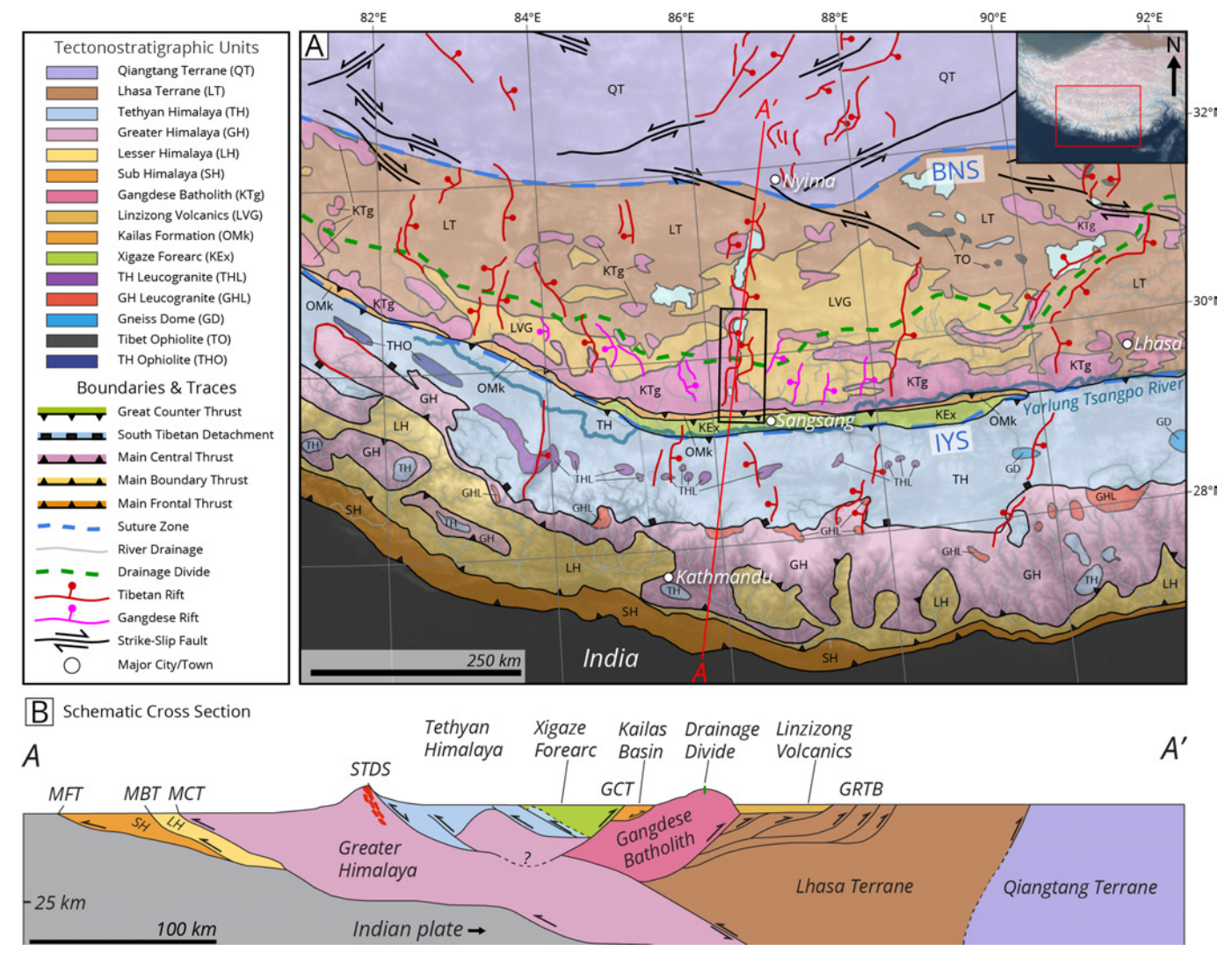


Figure 2 – (A) Geologic Map of the south-central Tibetan Plateau showing major tectonostratigraphic units and bounding faults, locations of Tibetan rifts (red) and Gangdese rifts (pink), as well as river drainages (gray), the Yarlung Tsangpo River (dark blue), and the Gangdese drainage divide (green). The black box shows the extent of geologic mapping in the southern TYC rift (Figure 4). Dashed blue lines = suture zones; BNS = Bangong-Nujiang suture; IYS = Indus-Yarlung suture. Fault traces from HimaTibet database (Styron et al., 2010). Geologic contacts adapted from Yin (2006). (B) Cross section interpretation based on the geologic map from (A).

and has remained at this relatively constant length through time, predicting uniform fault distribution and timing of extension onset along strike. These kinematic models provide a point of comparison for observed distributions of ZHe ages in the TYC rift and Gangdese rifts, allowing us to interpret rift initiation and fault growth behavior along strike.

1.2 Rift Timing

Early studies suggest rift initiation occurred synchronously across Tibet during Miocene time (ca. 14-8 Ma, Molnar et al., 1993; Turner et al., 1993; Harrison et al., 1995; Coleman and Hodges, 1995), but recent studies have shown rifting may have begun earlier and was diachronous across Tibet, with most graben systems initiating between 16 and 8 Ma (e.g., Armijo et al., 1986; Blisniuk et al., 2001; Williams et al., 2001; Murphy et al., 2010; Ratschbacher et al., 2011; Styron et al., 2011; Laskowski et al., 2017; Wolff et al., 2019, 2023; Burke et al., 2021; Bian et al., 2022). The

Tangra Yumco rift is one of the longest (\sim 250 km) and most centrally located rifts in Tibet, spanning the entire N-S length of the Lhasa terrane (Figure 1; Armijo et al., 1986; Taylor et al., 2003; Wolff et al., 2019, 2023). Active faulting in TYC is evidenced by well-developed triangular facets in fault footwalls and offset Quaternary sedimentary deposits in the rift hanging wall (Armijo et al., 1986; Wolff et al., 2019, 2023). Prior timing constraints for the TYC rift published by Wolff et al. (2019) include three samples from a footwall granite intrusion in northern TYC, two of which yielded concordant igneous U-Pb ages of 86.6 \pm 0.6 and 87.2 \pm 0.6 Ma and average zircon (U-Th)/He (ZHe) ages of 12.5 \pm 1.1 and 9.7 \pm 0.7 Ma. Wolff et al. (2023) published four additional footwall samples from the southern end of TYC yielding mean ZHe ages between 16.7 \pm 1.0 Ma and 13.3 \pm 0.6 Ma. Thermo-kinematic modeling in Pecube (Braun, 2003; Braun et al., 2012) indicated initiation of normal faulting in northern TYC at 14.5 \pm 1.8 Ma at a rate

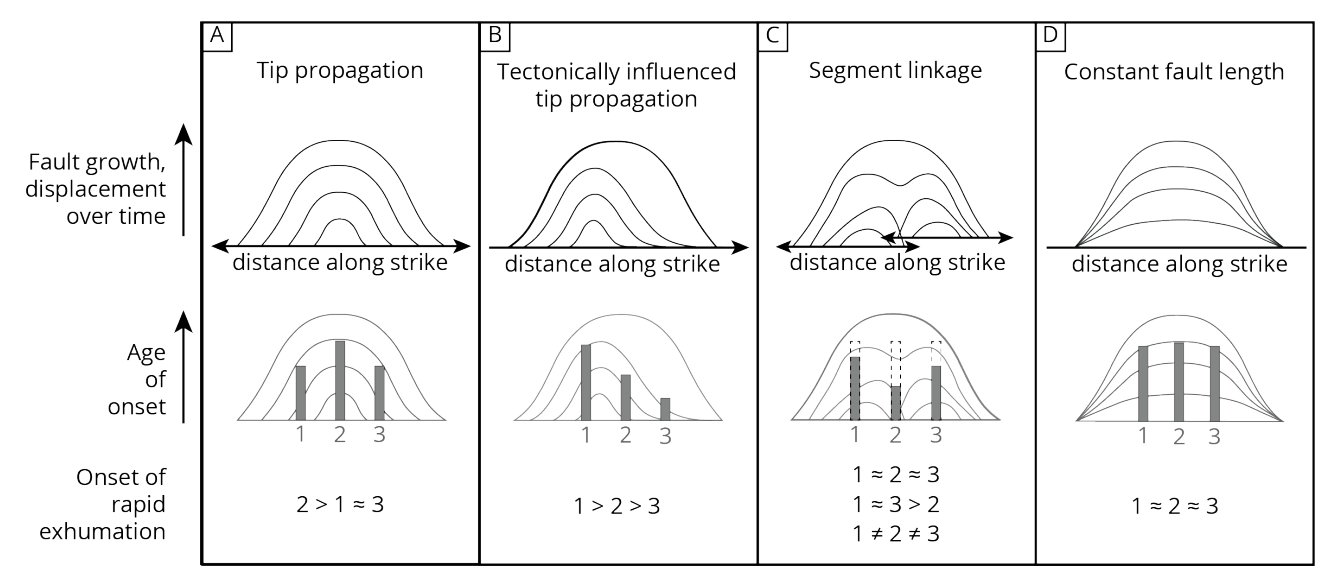


Figure 3 - Proposed kinematic models for normal fault growth; (A) Tip propagation, (B) Tectonically influenced tip propagation, (C) Segment Linkage, and (D) Constant fault length. Each model predicts specific map patterns of fault displacement over time (top row) and relationships for age of extension onset (bottom row). Onset of rapid exhumation is determined from age-elevation profiles of samples at different locations along-strike. Thick horizontal lines indicate fault traces and fault propagation through time (arrows), thin black and gray lines illustrate evolving lateral displacement profiles, vertical gray bars represent age of onset (greater bar height = older age of onset) for hypothetical along-strike sample transects (1, 2, 3). Dashed bars (C) represent variability in onset age due to fault segment initiation at variable times. Figure modified from Curry et al. (2016).

of \sim 0.2-0.3 mm/yr, which accelerated to \sim 0.6-0.8 mm/yr after ca. 3 Ma, whereas modeling of samples from southern TYC suggest initiation of rifting at 19.0 \pm 1.1 Ma at a rate of \sim 0.2 mm/yr, accelerating to \sim 0.4 mm/yr at ca. 5 Ma (*Wolff et al.*, 2019, 2023). Both studies interpret a two-phase cooling history for northern TYC, with an initial phase of slow cooling in the mid-Miocene followed by rapid cooling during Pliocene time (Wolff et al., 2019, 2023), with the latter responsible for the modern topography of the TYC rift. A northward-younging trend in the timing of rift acceleration has also been proposed for other Tibetan rifts where along-strike fault timing is well constrained (section 2.2.4 Tibetan Rifts; Styron et al., 2013; Sundell et al., 2013; Bian et al., 2022).

1.3 **Development of the Gangdese Drainage Divide**

Tectonically driven spatial and temporal variations in rates of rock uplift within active mountain belts has the potential to drive dynamic reorganization of fluvial networks and the drainage divides that bound individual network component (Willett et al., 2014). The internally drained portion of the Tibetan Plateau forms a long wavelength depression that is \sim 600,000 km² in size (*Fielding et al.*, 1994), with its southern boundary and the modern-day drainage divide marked by the crest of the Gangdese Range East-West extension in central and (Figure 2). southern Tibet is proposed to have initiated in the mid-Miocene (ca. 18 Ma, Li et al., 2015) or coeval with N-S shortening during Eocene time (ca. 47 Ma, Wang et al., 2010). East-West extension and strike-slip faulting have been suggested as likely contributors

to the diversion of river networks and relocation of lake centers in central Tibet since Miocene time (e.g., Han et al., 2019). Delamination, lithospheric dripping, and other deep crustal or mantle processes may enhance basin subsidence in central Tibet (*Gao* et al., 2013; Yin and Taylor, 2011; Bischoff and Flesch, 2018; *Han et al.*, 2019; *Kapp and DeCelles*, 2019), acting simultaneously to the already complex interplay between uplift, erosion, sedimentation, and climate to drive topographic change (e.g., Sobel and Strecker, 2003).

2 Regional Geologic Background

2.1 **Rock Units**

Rocks exposed in the southern TYC geologic map area and mapped in Figure 4 include: (1) Permian sedimentary units of the Lhasa terrane (brown), (2) Late Cretaceous-Paleogene calc-alkaline intrusive rocks (pink) of the Gangdese (Trans-Himalaya) magmatic arc, herein referred to as the Gangdese Range, (3) nonmarine sedimentary, volcanic, and volcaniclastic rocks (yellow) of the Linzizong Volcanic Group (LVG), (4) Cretaceous-Paleogene marine and nonmarine strata of the Xigaze forearc basin (green), and (5) Oligocene-Miocene nonmarine Kailas (Gangrinboche) Formation conglomerates (light orange). Permian sedimentary rocks exposed in the central and northern map area (Figure 4), include the Angjie and Luobadui Formations consisting of dark gray slate, fine grained quartz sandstone, siltstone, mudstone, and limestone (e.g., Geng et al., 2009) and shallow-marine fossiliferous limestones, terrigenous sediments, and intercalated volcanic

rocks (Wang et al., 2022), respectively. Fossils of the Luobadui Formation including abundant brachiopods, bryozoans, fusulinids, and corals indicate middle Permian deposition, likely related to southward subduction of the Paleotethys (*Geng et al.*, 2009; Kapp and DeCelles, 2019) with recent dating of volcanic rocks constraining the Luobadui Formation to between ca. 275-260 Ma (Wang et al., 2022).

Gangdese Range rocks (pink, Figure 4) are composed of calc-alkaline intrusive granites and granodiorites (e.g., He et al., 2007; Ji et al., 2009; Zhu et al., 2011). Episodic magmatic activity in the Gangdese Range occurred between ca. Ma and ca. 40 Ma, with a highest magmatic flux occurring at ca. 52 Ma (e.g., Zhu et al., 2011; Leary et al., 2016) and relatively low-volume magmatism continuing as late as ca. 8 Ma (Zhu et al., 2011; Zhang et al., 2014; Leary et al., 2016). Rocks of the Gangdese batholith and LVG are interpreted to be genetically linked (e.g., Leary et al., 2016) with their formation likely driven by continental arc magmatism related to northward subduction and/or breakoff of Neo-Tethyan lithosphere in the Late Cretaceous-Paleogene (Schärer et al., 1984; Pan et al., 2004; Lee et al., 2007, 2009; Liu et al., 2018; Kapp and DeCelles, 2019).

The Linzizong Volcanic Group (yellow, Figure 4) is subdivided into the lower Dianzhong (60.2-58.3 Ma), middle Nianbo (55.4-52.6 Ma), and upper Pana (52.6-52.3 Ma) Formations (*Zhu et al.*, 2015), consisting mainly of porphyritic andesite with minor basalt, dacite, rhyolite, and tuffaceous lavas (*Mo et al.*, 2008; Lee et al., 2012; Liu et al., 2018; Huang et al., 2013; *Zhu et al.*, 2015; *Zhang et al.*, 2022). The Nianbo Formation is spatially variable in deposition in central Tibet, thus the Pana Formation may unconformably overly the Dianzhong Formation or Angjie Formation in this region.

At the southernmost end of the TYC rift (Figure 4), the Cretaceous Ngamring Formation (Wu et al., 1977) of the Xigaze Forearc Group (green) is observed in fault contact with the Dazhuka Formation of the Oligocene-Miocene Kailas Group (light orange) along a steeply south-dipping reverse fault (Wang et al., 2012; An et al., 2014; Orme et al., 2015; Orme and Laskowski, 2016; Orme, 2019). The Ngamring Formation has been dated to ca. 107-84 Ma (Wu et al., 2010), is between 1000-4100 meters thick, and contains a series of fining-upward deep-marine turbidite sequences interbedded with marine and nonmarine sedimentary units (Einsele et al., 1994; Dürr, 1996; Wang et al., 2012; An et al., 2014; Orme and Laskowski, 2016).

The Kailas Formation is spatially variable in depositional age and thickness and is referred to by different names across the IYS, including the Kailas, Qiuwu, Dazhuka and Luobusa Formations (Heim and Gansser, 1975; Gansser, 1964; Aitchison et al., 2002; DeCelles et al., 2011; Li et al., 2017; Zhang et al., 2017; Laskowski et al., 2018). A west-to-east trend in depositional age for the Kailas Formation was recognized by *Leary et al.* (2016), varying from 26-24 Ma near Mt. Kailash (\sim 81.3°E) to 23-22 Ma near Dazhuka (~89.6°E). The Dazhuka Formation is equivalent to the geographically central portion of the Kailas Formation and is comprised of dark gray to gray-green conglomerates with clasts of granite, gneiss, ultra-mafic and mafic rocks, lithic sandstone and siltstone, and minor rhyolite (Aitchison et al., 2002; Wang et al., 2013; Huang et al., 2019). The Dazhuka Formation typically overlaps, forms an angular unconformity, or is faulted onto rocks of the LVG or Gangdese batholith (Gansser, 1964; Leary et al., 2016; Laskowski et al., 2018). It is proposed that anchoring or rollback of the Indian slab (e.g., Replumaz et al., 2010) at ca. 26 Ma may have reactivated the IYS as a north-dipping normal fault to accommodate N-S extension and deposition in the Kailas basin until ca. 21 Ma (DeCelles et al., 2011, 2016; Wang et al., 2013; Leary et al., 2016; Laskowski et al., 2017, 2018; Kapp and DeCelles, 2019). Alternatively, the Kailas Basin may be the product of dynamic subsidence related to southward folding of the Indian Slab (Husson et al., 2014; Shen et al., 2020).

Finally, Paleocene-Eocene porphyritic rhyolite intrusions (Eqλ, Figure 4) related to the Chagele deposits of the Gangdese Metallogenic Belt (\sim 63-32 Ma, Hou et al., 2004; Gao et al., 2021) and north trending dikes from the Daggyai Tso graben (recently referred to as the Dajiamang Tso rift; Burke et al., 2021) located \sim 50 km west of TYC yielded U-Pb ages of ca. 18-13 Ma consistent with studies suggesting a minimum age of \sim 18 Ma for the onset of east-west extension in southern Tibet (Williams et al., 2001; McCallister et al., 2014; Burke et al., 2021).

2.2 Fault Systems

2.2.1 Gangdese Retroarc Fold-Thrust Belt

A contractional Cordilleran-style retroarc thrust belt north of the Gangdese Range in the Lhasa terrane has been interpreted based on the presence of an angular unconformity separating highly shortened Permian-Cretaceous strata from overlying weakly deformed Cretaceous-Tertiary rocks of the LVG (e.g., Burg et al., 1983; England and Searle, 1986; Ratschbacher et al., 1992; Kapp et al., 2007; Leier et al., 2007). To the west near Lhasa city, contractional structures likely related to the Gangdese Retroarc Fold-Thrust Belt (GRTB) are thought to have accommodated >230 km of N-S shortening between 105 and 53 Ma (Kapp et al., 2007). Retroarc shortening ceased at ca. 55–50 Ma, roughly coeval with the initiation of India-Asia collision in southern Tibet and a southward sweep of magmatism across the Lhasa terrane, possibly reflecting a decrease in India-Asia convergence rates and rollback of the Neotethyan slab (e.g., Patriat and Achache, 1984; Zhu et al., 2005; Kapp et al., 2007; Kapp and DeCelles, 2019).

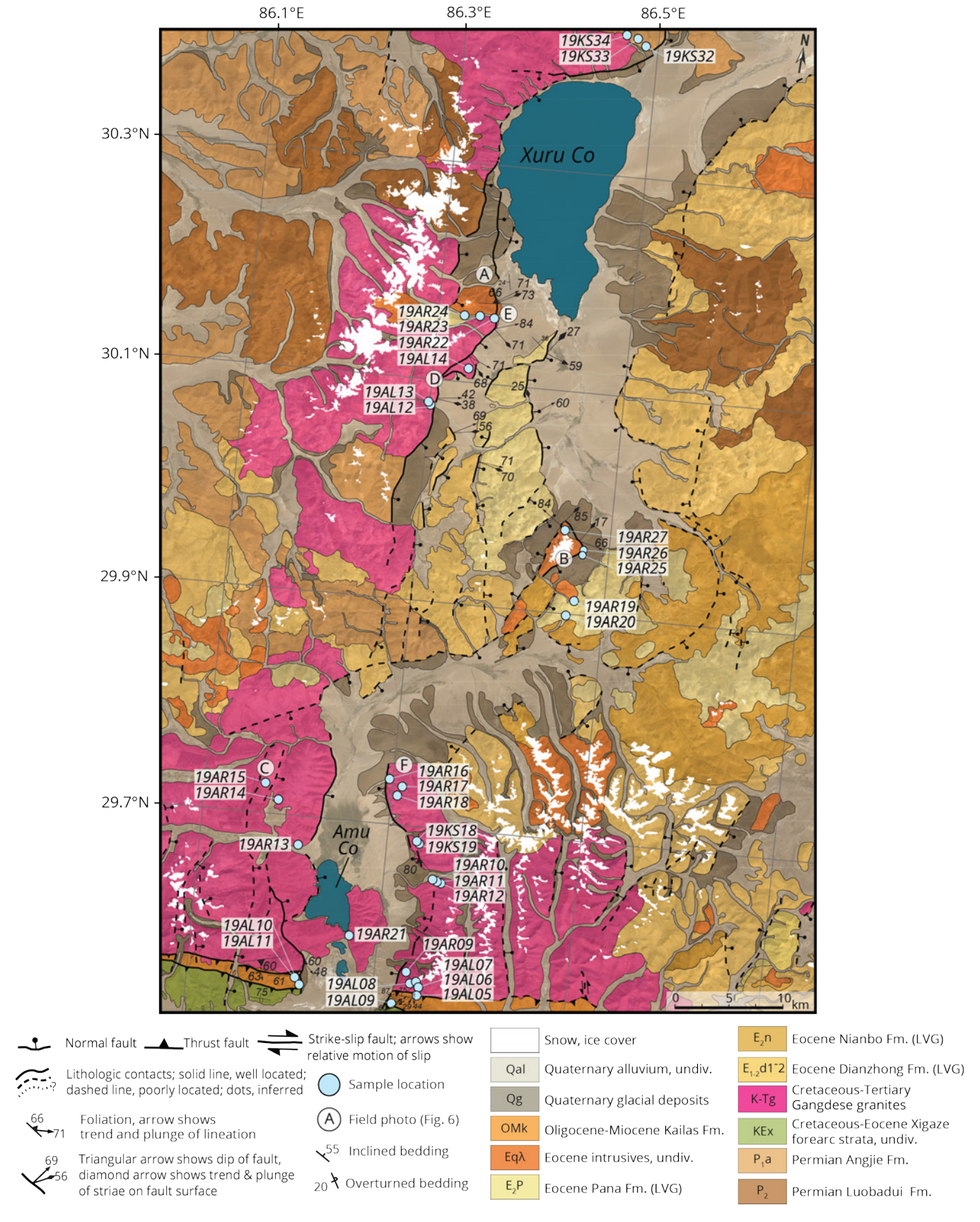


Figure 4 – Geologic map of the southern Tangra Yumco rift. Mapping was conducted at \sim 1:100,000 scale including field observations supplemented by digital mapping from satellite imagery and previous geologic mapping at 1:250,000 scale (*Pan et al.*, 2004). Geologic contacts were interpolated in difficult to access areas and between field traverses using Google Earth and Landsat imagery, as extreme elevations (>6000 m), snow and ice cover, and limited roads prohibited complete access to the map area. Mapped features were drafted over hill shade and slope maps with topography derived from Shuttle Radar Topography Mission (SRTM) 1 Arc-Second Global Digital Elevation data (DOI: 10.5066/F7PR7TFT) and draped Landsat Legacy Global Land Survey (GLS) imagery (DOI: 10.5066/F7M32TQB).

2.2.2 Gangdese Thrust

The north-dipping Gangdese Thrust (GT) system was first interpreted by Yin et al. (1994) to place Cretaceous Xigaze Group forearc basin strata over Tethyan sedimentary rocks near the town of Xigaze (~250 km east of southern TYC), and Gangdese batholith rocks over Tethyan rocks to the east of Lhasa city near Zedong. Since then, many of the contacts near Xigaze have been revisited and interpreted to be predominantly related to the Great Counter Thrust system (e.g., Murphy et al., 2010; Leary et al., 2016; Laskowski et al., 2018). Evidence of the GT as defined in previous studies was not observed in the area of this study, but if the GT or equivalent structure were present at the surface or at depth, it would likely have been active between ca. 23-13 Ma, overlapping the estimated timing of Great Counter Thrust system (Tremblay et al., 2015; Laskowski et al., 2018).

2.2.3 The Great Counter Thrust System

The IYS and Xigaze forearc are cut by a series of north-vergent, generally south-dipping (locally overturned) thrust faults known as the Great Counter Thrust system (GCT, e.g., Heim and Gansser, 1975; Yin et al., 1994, 1999a; Murphy et al., 2010). The GCT is the northernmost fault system of the broader Tethyan Himalayan thrust belt, representing the northernmost extent of Himalayan fold-thrust belt deformation (Leary et al., 2016; Laskowski et al., 2018). The GCT places Tethyan Himalaya rocks over IYS rocks, and Xigaze forearc rocks over Kailas Formation conglomerates (Leary et al., 2016; Laskowski et al., 2017, 2018). The GCT likely initiated during the latest Kailas Formation sedimentation (~21 Ma) based on a shift in paleocurrents, clast compositions, and crosscutting relationships (DeCelles et al., 2011; Leary The lower limit on GCT activity is et al., 2016). constrained by the shift from N-S contraction to E-W extension in southern Tibet and is recorded by the initiation of Tibetan rifts which crosscut the GCT $(\sim 18-13 \text{ Ma})$ (Ratschbacher et al., 1994; Harrison et al., 2000; Yin et al., 1994, 1999a; Murphy et al., 2010; Sanchez et al., 2013; Styron et al., 2013; Leary et al., 2016; *Laskowski et al.*, 2017, 2018).

2.2.4 Tibetan Rifts

Tibetan rifts are predominantly located in the Lhasa Terrane and commonly >150 km in N-S length and spaced \sim 146 \pm 34 km apart, facilitating east-west extension and crosscutting several of the previously described pre-Cenozoic contractional structures of the Tibetan Plateau (Figure 1 and 2; Armijo et al., 1986; Yin, 2000; Burke et al., 2021). Here we compile relevant field observations and timing constraints from four additional rifts of the seven major Tibetan rift systems that crosscut the Lhasa terrane (Figure 1) including the Lunggar (7, 8), Lopu Kangri (9), Pumqu-Xainza (5, 12), and Yadong-Gulu (6, 13) rift systems. We compare these results to

observations and timing constraints for the Tangra Yumco rift (described in section 1.1. Rift Initiation) and additionally, provide a general review of lesser studied Tibetan rifts systems located south of the IYS and north of the BNS.

The Lunggar rift system is located \sim 300 km west of TYC (Figure 1) and has been studied extensively in the south (Styron et al., 2013) and north (Kapp et al., 2008; Sundell et al., 2013). Unlike many of the high-angle rift systems in south-central Tibet and the Himalaya, motion along the Lunggar rift is dominated by two low-angle normal faults, the east-dipping North Lunggar Detachment (NLD) and west-dipping South Lunggar Detachment (SLD), which exhume Miocene leucogranites (ca. 15-9 Ma; Kapp et al., 2008) and mylonitic shear zones in their footwalls (Kapp et al., 2008; Styron et al., 2013; Sundell et al., 2013). Normal faulting in the South Lunggar Rift initiated during the mid-Miocene between ca. 16-12 Ma with relatively slow horizontal extension rates (\sim 1 mm/yr) and accelerated in the north at ca. 8 Ma (\sim 2.5-3.0 mm/yr; Styron et al., 2013). Thermal history modeling of ZHe and AHe data yielded a minimum timing for North Lunggar Rift initiation of >10 Ma with initially slow rates of cooling (<50 °C/Myr) and exhumation (<1 mm/yr), followed by rapid footwall cooling (>400 °C/Myr) and exhumation (4-10 mm/yr) between 5-2 Ma (Sundell et al., 2013), suggesting synchronous rift initiation during the mid-Miocene followed by a northward sweep of rift acceleration in the late Miocene to Pliocene (Styron et al., 2015).

Lopu Kangri is located ∼150 km west of TYC at its southern extent (Figure 1) and exposes a continental high-pressure metamorphic complex beneath IYS assemblages (Laskowski et al., 2017). Two N-S striking range-bounding faults, the Lopukangri and Rujiao faults, comprise a horst block which crosscuts the Great Counter Thrust system. Seven ZHe ages from the horst block suggest cooling between ca. Ma and ca. 6.0 Ma and potentially recording the early Miocene (~16 Ma) transition from north-south contraction to E-W extension in this region (Laskowski et al., 2017). These results are consistent with the findings of numerous studies revealing middle Miocene (\sim 16 Ma) extension onset followed by a late Miocene-Pliocene acceleration of exhumation.

The Pumqu-Xainza (PQX) rift system (also known as the Dinggye-Xainza rift) is ~350 km long and located ~190 km east of TYC at its southern extent (Figure 1). The southernmost portion of the rift (Pumqu/Dinggye) intersects and cuts across the IYS and South Tibetan Detachment system (STDS), extending as far south as \sim 50 km north of the Main Frontal Thrust, while the northernmost part of the rift (Xainza) intersects the right-lateral Gyaring Co strike-slip fault ~130 km south of the BNS (Zhang et al., 2002; Zhang and Guo, 2007; Wang et al., 2014; Sheng et al., 2021). Structural observations and timing estimates for PQX are consistent with extension initiation since 14 Ma with maintained activity to the Pleistocene (Zhang et al., 2002).

The Yadong-Gulu rift system (YGR) is located \sim 360 km east of TYC (Figure 1) and has also been studied extensively in its south (Yadong) and north (Gulu) segments (Armijo et al., 1986; Pan and Kidd, 1992; Cogan et al., 1998; Wu et al., 1998; Stockli et al., 2002; Kapp et al., 2005; Wu et al., 2015; Ha et al., 2019; Chevalier et al., 2019; Bian et al., 2022). YGR extends \sim 500 km from near the China-India (Sikkim) border in the south to Naggu in the north, crosscutting major geological structures including the South Tibetan Detachment System (STDS, e.g., Burchfiel et al., 1992) and the IYS before tracing the east side of the Nyaingentanghla Range and intersecting a right-lateral strike slip fault south of the BNS (Chevalier et al., 2019). Like the Lunggar rift, the YGR is a low angle structure exposing a mylonitic shear zone and Miocene granites in its southern footwall, documenting significant and rapid exhumation during Pliocene time (*Kapp et al.*, 2008). Recent thermochronology data from YGR indicate a generally northward younging trend in the timing of rift initiation, from ca. 13-11 Ma in southern Tibet 7-5 Ma in the northern rift, suggesting a northward propagation of rift initiation (Bian et al., 2022). The YGR's variable along-strike timing of rift initiation could perhaps be attributed to its more oblique orientation and farther eastward location (Bian et al., 2022) or variations in the shape, angle, and extent of the subducting Indian plate, an idea which was also recently considered for the TYC rift (Wolff et al., 2023).

Extensional systems south of the IYS include Gurla Mandhata, Thakkhola, Kung Co, and the southern portions of the Pumqu/Dinggye rift and Yadong rift (Figure 1), with greater spacing between each of the rift systems than is observed in the Lhasa Terrane (i.e., greatest rift spacing in the Himalaya and smallest spacing north of the BNS). Three of the rifts (Thakkhola, Pumqu, and Yadong) are unusual in that they extend farther south to cross the Himalayan Range (Chevalier et al., 2019). Generally, the timing of initiation along rifts south of the IYS is interpreted to have occurred by mid-Miocene (~16-14 Ma) time (e.g., Murphy et al., 2002; McCallister et al., 2014; Coleman and Hodges, 1995; Maheo et al., 2007; Lee et al., 2011; Jessup et al., 2008; Kali et al., 2010; Ratschbacher et al., 2011). Of particular interest, the Kung Co rift is located ∼100 km NW of Mount Everest (Qomolangma; Figure 1) and directly south of where the TYC rift cuts the IYS (e.g., Maheo et al., 2007; Wolff et al., 2019, 2023; Chevalier et al., 2019). Inverse modeling of thermochronology data from Kung Co indicates slip initiation at \sim 13–12 Ma with rapid footwall exhumation between ~13-10 Ma and an acceleration of slip rates at \sim 10 Ma (*Maheo et al.*, 2007; Lee et al., 2011).

North of the BNS, a general decrease in rift spacing and length (<100 km apart) has been suggested to reflect differing mechanical properties of the Lhasa

and Qiangtang Terranes (e.g., Armijo et al., 1986; The mechanisms of extension also appear to differ from those south of the BNS, with eastward extension north of the BNS dominated by motion along strike-slip faults with rifts system displaying lesser offsets and subdued morphological expressions (e.g., Taylor et al., 2003; Chevalier et al., 2019). Though there are few detailed studies of rift systems north of the BNS, observations from the Shuanghu rift in the central Qiangtang Terrane (Figure 1) including fault geometry and kinematics suggest that the rift bounding faults activated periodically, with early activity in the late Miocene (\sim 13.5 Ma; *Blisniuk et al.*, 2001) to Pliocene followed by an increase in rift rates since the Quaternary, with slip estimates comparable to estimates for equivalent structures in southern Tibet (*Yin et al.*, 1999b; *Li et al.*, 2001).

Observations from various Tibetan rifts reveal key similarities with the Tangra Yumco rift. The suggested timing of rift initiation in the mid-Miocene and subsequent northward sweep of rift acceleration in the late Miocene to Pliocene has been proposed for many of the rift systems, suggesting they have at least in some part a common mechanism of origin and evolution (DeCelles et al., 2002; Kapp et al., 2005; Styron et al., 2015; Wolff et al., 2019, 2023; Bian et al., 2022). Multiple other rifts are kinematically linked to a dextral strike slip fault to the north near the Bangong-Nujiang Suture Zone, which further suggests a common evolution (Armijo et al., 1986; *Taylor et al.*, 2003; *Wolff et al.*, 2019, 2023). Finally, an intra-basin high is observed in multiple rift systems, and in central TYC forms a drainage divide, causing river systems to flow into one of three distinct lakes within the rift basin; Tangra Yum Co in the north, Xuru Co in the center, and Dajia Co in the south (Wolff et al., 2023). Tangra Yum Co and Xuru Co lakes are situated within the internally drained portion of the plateau (i.e., north of the drainage divide), whereas Dajia Co is located south of the divide and drains into the Dogxung-Tsangpo river, a tributary of the Yarlung-Tsangpo river (Figure 2 Wolff et al., 2023), which is similar to drainage divide patterns observed in the other Tibetan rift systems.

2.2.5 Gangdese Rifts

Gangdese rifts are defined as shorter than 150 km in length, are closely spaced (\sim 46 \pm 7 km), and are isolated within the high topography of the Gangdese Range along the southern margin of the Lhasa terrane (Figures 1 and 2; Yin, 2000; Burke et al., 2021). Gangdese rifts are typically horst-and-graben structures, with the high relief horsts bounded by high-angle active east-dipping and west-dipping normal faults. Recently published geoand thermochronology results from the Dajiamang Tso rift constrain the age of extension onset to between 16-8 Ma (Burke et al., 2021). A minimum age of ca. 16 Ma for extension onset is consistent (within \pm 2 Ma) with results from other rifts (*Yin*

and Harrison, 2000; Williams et al., 2001; McCallister et al., 2014; Sanchez et al., 2013; Laskowski et al., 2017). U-Pb dating of north trending extensional dikes of the Daggyai Tso graben (the northern portion of the Dajiamang Tso rift) yielded ages between 18-13 Ma (Williams et al., 2001; McCallister et al., 2014). 40Ar/39Ar results dating movement along the Lopu Kangri rift (Sanchez et al., 2013; Laskowski et al., 2017) and north striking mineralized fractures near the Thakkhola graben (Murphy et al., 2010) yielded ages of \sim 15 Ma and \sim 14 Ma, respectively. Furthermore, active extension and exhumation along the high-angle normal faults that border the Lopu Kangri rift are evidenced by young ZHe cooling ages and well-formed triangular facets and quaternary alluvial deposits cut by fault scarps (Laskowski et al., 2017), as well as seismogenic activity (*Zhang et al.*, 2004; Gan et al., 2007).

3 Methods

3.1 Geologic Mapping

Geologic mapping was conducted in the southern Tangra Yumco rift, ~40 km northwest of the city of Sangsang, Tibetan Autonomous Region, China (Figure 2). Sangsang is located ~430 km west of Lhasa and ∼160 km north of Mt. Qomolangma (Everest, Figure 1). Geologic mapping followed a 'mapping mode' workflow in the StraboSpot digital geologic data system application for iOS; geologic features were recorded by direct observation in the field at scales locatable by GPS (Walker et al., 2019). Mapping was conducted at \sim 1:100,000 scale across the study area within the southern TYC rift (Figure 4). Field mapping was supplemented with digital mapping from satellite imagery and previous existing regional geologic mapping at 1:500,000 scale (Pan et al., 2004). Mapped features were drafted over hill shade and slope maps derived from Shuttle Radar Topography Mission (SRTM) 1 Arc-Second Global Digital Elevation data (DOI: 10.5066/F7PR7TFT) and draped Landsat Legacy Global Land Survey (GLS) imagery (DOI: 10.5066/F7M32TQB). Geologic contacts were interpolated in difficult to access areas and between field traverses using Google Earth and Landsat imagery, as extreme elevations (>6000 m), snow and ice cover, and limited roads prohibited complete access to the map area. Digitally mapped features were interpreted based on tonal variations in satellite imagery, presence of triangular facets, mountain front sinuosity, linearity of features (e.g., fault scarps), and deflected streams, rivers, and drainages.

3.2 Zircon U-Pb Geochronology

Eighteen of fifty samples collected from rift footwall transects were selected for zircon U-Pb geochronology to constrain the crystallization age for footwall rocks along strike of the TYC rift (location and lithology data for each sample are provided in

Table 1; Reynolds, 2023). Zircons were extracted from bulk samples using standard crushing, sieving, electro-magnetic, and heavy liquid mineral separation techniques. Zircon grains for each sample (n = 75) were mounted in 1 inch epoxy ring forms alongside Sri Lanka (SLmix), R33, and FC zircon standards (Paces and Miller, 1993; Schmitz et al., 2003; Black et al., 2004; Gehrels et al., 2008), then polished to a depth of \sim 20 μm at the Tectonic Sedimentology and Thermochronology (TeST) laboratory at Montana State University. Backscattered electron (BSE) cathodoluminescence (CL) imagery was obtained for each sample prior to analysis at the University of Arizona LaserChron Center (ALC) to provide generalized maps for isotopic analysis and targeting of specific age domains. Zircon U-Pb geochronology was conducted at ALC following the detailed analytical procedures and data reduction methods of Gehrels et al. (2006, 2008) and Pullen A Photon Machines Analyte G2 et al. (2018). Excimer laser attached to a Thermo Element2 HR single-collector ICP-MS was used to measure U, Th, and Pb isotopes. Analytical uncertainties related to determination of ²⁰⁶Pb/²³⁸U and ²⁰⁶Pb/²⁰⁴Pb are between 1-2% (2σ) for individual reported ages. Standard sample bracketing with SLmix, R33, and FC zircon reference materials of known age were used to correct for inter-element fractionation of U and Pb isotopes (Gehrels et al., 2008). U-Pb weighted mean age determinations reject and exclude from visual representation all U-Pb analyses with >20% discordance or >5% reverse discordance. The AgePick Excel Tool available online from ALC (Gehrels, 2009) was utilized to calculate the reported weighted mean age, uncertainty, and MSWD for each sample. An MSWD = 1 indicates the degree of scatter is consistent with analytical precision. Weighted mean plots were generated using the AgeCalcML Weighted Mean Plotter (Sundell et al., 2020, Figure S2). Analyses for spots recording >1000 ppm U or ages exceeding 2 σ error on weighted mean plots are considered outliers based on Chauvenet's criterion (e.g., Vermeesch, 2018), and therefore these analyses were systematically excluded from AgePick calculations, data visualizations, and subsequent interpretation. Reported ages reflect systematic error including standard calibration, age of the calibration standard, composition of common Pb, and the 238 U decay constant, and is generally \sim 1–2% at the 2σ level (Gehrels et al., 2009). Full analytical details and U-Pb results for each sample are provided in supplementary data Table S2 (Reynolds, 2023). Weighted mean plots for all samples are included in supplementary Figure S2.

3.3 Zircon (U-Th)/He Thermochronology

Fifty igneous samples were collected for zircon (U-Th)/He (ZHe) dating. We utilize ZHe dating because it generally records cooling over a closure temperature range of \sim 140-220 °C (*Guenthner et al.*, 2013) and is well suited to investigate tectonic

Table 1 – Sample Location and Lithology

Sample Name	Latitude (°N)	Longitude (°E)	Elevation (m)	Lithology	Unit abv.	Mean ZHe Age (Ma)	$\pm 1\sigma$	Mean U-Pb Age (Ma)	$\pm 1\sigma$
19AL05	29.54241	86.34583	5507	Lithic Sandstone	OMk	19.90	0.25	Age (Ma)	
19AL06	29.54879	86.3457	5855	Granodiorite	Gg	22.72	0.31	53	0.11
19AL07	29.55293	86.3443	5786	Granodiorite	Gg	20.40	0.25	54.62	0.014
19AL08	29.55096	86.33735	5608	Granodiorite	Gg	17.89	0.23	56.15	0.21
19AL09	29.52943		5002	Lithic Sandstone	KPq	26.10	0.34	30.13	0.21
19AL10	29.55081	86.21104	5058	Quartz Sandstone	KPq	21.28	0.27		
19AL11	29.54633	86.21975	4963	Conglomerate	KPq	22.23	0.31		
	30.079375		5011	Porphyritic Rhyolite	•	41.47	0.52		
	30.079922		5052	Porphyritic Andesite		43.96	0.67		
19AL14	30.11307	86.33408	5161	Porphyritic Andesite	KPlz	54.00	0.73		
19AL15		86.667312	4675	Granodiorite	Gg	28.29	0.42		
	29.640538		5036	Granodiorite	Gg	28.30	0.36		
	29.808505		5006	Porphyritic Andesite		44.68	0.53		
19AR01		87.033703	4817	Granodiorite	Gg	18.23	0.22		
	29.498585		5171	Granodiorite	Gg	15.79	0.20		
19AR03	29.4854	87.02821	5318	Granodiorite	Gg	20.13	0.26		
	29.410081		4379	Porphyritic Andesite		16.38	0.22	50.95	0.1
	29.423917		4410	Granodiorite	Gg	27.98	0.35	30.33	011
	29.434158		4442	Granodiorite	Gg	24.87	0.32		
19AR07	29.4663	87.1517	4546	Granodiorite	Gg	20.33	0.24	49.75	0.12
19AR08	29.50104	87.15913	4722	Granodiorite	Gg	19.70	0.24	50.51	0.15
	29.562388		5374	Granodiorite	Gg	14.84	0.21	30.3	01.15
	29.648425		5367	Granodiorite	Gg	17.38	0.23	53	0.14
19AR11	29.64826	86.352092	5424	Porphyritic Andesite		14.86	0.19	16.18	0.03
-	29.647433		5524	Granodiorite	Gg	15.84	0.20	54	0.19
	29.667639		5000	Granodiorite	Gg	18.94	0.25		
	29.706723		5324	Granodiorite	Gg	20.16	0.26		
	29.720758		5536	Granodiorite	Gg	15.95	0.20	50.18	0.14
19AR16	29.735243	86.290704	4957	Granodiorite	Gg	18.77	0.22	49.41	0.12
	29.729595		5212	Granodiorite	Gg	21.87	0.27	49.92	0.14
19AR18	29.721146	86.304421	5109	Granodiorite	Gg	19.36	0.24	49.76	0.14
19AR19	29.913056	86.46747	5489	Felsic Tuff	KPlz	53.66	0.67		
19AR20	29.898924	86.459042	5282	Porphyritic Andesite	KPlz	45.48	0.60		
19AR21	29.590239	86.269258	4776	Granodiorite	Gg	28.04	0.36		
19AR22	30.162284	86.355441	5043	Granodiorite	Gg	4.72	0.06		
19AR23	30.1626	86.34021	5217	Granodiorite	Gg	24.56	0.31		
19AR24	30.161614	86.323944	5275	Porphyritic Andesite		8.98	0.12	58.9	0.17
19AR25	29.958542	86.467537	5615	Porphyritic Andesite	KPlz	8.11	0.10	10.79	0.01
19AR26	29.96012	86.4697	5539	Granodiorite	Gg	8.13	0.10	11.06	0.01
19AR27	29.9827	86.45224	5369	Granodiorite	Gg	8.83	0.11	56.06	0.26
19GR01	29.634465	87.065858	4949	Porphyritic Andesite		21.77	0.26		
19GR02	29.634643	87.073496	5329	Porphyritic Andesite		20.35	0.24		
	29.636049		5405	Porphyritic Andesite	KPlz	19.74	0.24		
19GR05		87.07273	5003	Porphyritic Andesite	KPlz	15.65	0.20		
19GR06		87.07893	5308	Porphyritic Andesite		20.90	0.26		
19GR07	29.64614	87.0834	5595	Porphyritic Andesite	KPlz	18.54	0.22		
	30.423606		4963	Granodiorite	Gg	49.79	0.63		
		86.477097	5307	Granodiorite	Gg	59.33	0.75		
	30.428588		5452	Granite	Gg	54.01	0.69	151.92	0.9
					U				

questions within the upper ~2-10 km of the Earth's crust. This range of possible depths accounts for variations in cooling rate that can affect the depth of the ZHe partial retention zone (PRZ), as well as variations in the closure temperature which is affected by factors such as the grain size and intensity of radiation damage within individual crystals (e.g., *Dodson*, 1973; *Reiners et al.*, 2002; *Reiners and Brandon*, 2006; *Ault et al.*, 2019; *Whipp et al.*, 2022). Sample transects were collected perpendicular to the strike of normal faults bounding the TYC and Gangdese rifts (Figures 2 and 4). Bulk samples underwent standard crushing, sieving, electro-magnetic, and heavy liquid mineral separation techniques at the Chinese Academy

of Sciences in Beijing, China. All but one sample (19AL14) yielded sufficient zircon separates suitable for ZHe analysis. Five zircon grains from each sample (245 total grains) were handpicked for analysis at the Montana State University Tectonic Sedimentology and Thermochronology (TeST) laboratory. Grains were selected based on morphology (subhedral to euhedral), size (diameter >60 μm), and clarity (minimal inclusions or fractures) to reduce grain size effects on intrasample age variation (Reiners Long and short axis grain and Farley, 2001). dimensions were measured from photomicrographs for α -ejection correction calculations (Farley et al., 1996) following procedures outlined in *Hourigan* et al. (2005). Grains were individually sealed into

1mm Nb foil packets to ensure even heating and prevent volitization of parent nuclides during helium extraction. Collection and measurement of 4He and isotopic dissolution to determine U-Th-Sm content was completed at the Arizona Radiogenic Helium Dating Laboratory (ARHDL) following the detailed procedures of *Reiners et al.* (2004) and *Reiners* (2005).

During analysis, individual packets were loaded into a vacuum laser cell and individually heated for 15 min using a focused beam from a 1-2W laser to extract 4He gas from the grain. A minimum of one re-extraction was completed for each zircon by reheating for 15-20 minutes, repeated until 4He extractions were 2% or less of the compounded 4He/3He ratios were measured using a quadrupole mass spectrometer equipped with a Channeltron electron multiplier. Fish Canyon Tuff (FCT) zircon standards with accepted ZHe age of 28.48 ± 0.06 (2 σ) Ma (Schmitz and Bowring, 2001) were analyzed between every 5–7 unknowns to account for changes in isotopic fractionation or sensitivity bias (*Reiners*, 2005). Parent concentrations (U, Th, and Sm) were measured by isotope dissolution and inductively coupled plasma mass spectrometry (ICP-MS) using appropriate acids (Reiners, 2005). Analytical uncertainties include systematic and measurement errors for ZHe ages typically on the order of 1–3% at 2σ (*Reiners et al.*, 2004). Analytical error includes the propagation of uncertainties from measurements such as grain size, 4He, U, Th, and Sm, but does not include errors associated with the alpha ejection correction which assumes homogenous parent nuclide distributions for individual grains (Hourigan et al., 2005). Detailed sample information and single grain ZHe analytical data are provided in supplementary Table S3 (Reynolds, 2023). Reported mean ages were determined by averaging 3-5 grains per sample to allow exclusion of outliers beyond acceptable error. We note intra-sample variability of effective uranium (eU = [U] + 0.235[Th]; Guenthner et al., 2013), a proxy for radiation damage within individual crystals, as well as minor variations in grain size and 4He content. Intra-sample variabilities are examined for potential structural context during interpretation of cooling ages.

3.4 HeFTy Thermal Modeling

Inverse modeling was conducted using HeFTy thermal modeling software program version 1.9.3 (*Ketcham*, 2005). HeFTy inverse models use measured cooling ages as inputs and produce a suite of time-temperature (t-T) paths containing predicted ages that might provide good or acceptable fits to measured ages. This allows the user to test thousands of potential thermal histories based on measured data and additional imposed search constraints in the model's time-temperature space to determine a path which best fits the known thermochronology and geologic data. HeFTy is based on a Monte-Carlo algorithm that accounts for the diffusive loss and radiogenic ingrowth of

4He for individual grains as a function of thermal history, and utilizes a frequentist approach, meaning that formal statistical hypothesis tests can assess the goodness-of-fit between user input data and thermal model predictions (Vermeesch and Tian, 2014). Interpreting t-T paths for samples across a broad study area can expose spatial trends in the timing and rates of exhumation, which may provide broader tectonic implications. Conversely, HeFTy forward models generate predicted cooling ages for a specified t-T history that is input by the user. Predicted cooling ages can then be iteratively compared with measured data to test a variety of hypothesized thermal histories. Forward models are useful for ruling out thermal histories based on geologic scenarios that are inconsistent with field observations or measured values and can reveal how grain-specific parameters (e.g., grain size, radiation damage, diffusion kinetics) might affect intra-sample age variability. In this study we have developed a large dataset of measured ZHe cooling ages and are interested in generating potential thermal histories based on these results; therefore we utilize inverse HeFTy models rather than forward HeFTy models. Inputs for inverse models include grain-specific measurements (grain radius, U and Th concentration, and uncorrected cooling age) which force model paths to pass through a known t-T point based on these parameters. Models can include additional imposed t-T constraints based on measured results from other geochronology or thermochronology systems (e.g., U-Pb crystallization ages to constrain the higher temperature range of predicted thermal histories) or known geologic relationships from field observations. Results for preliminary HeFTy thermal models are detailed in section 4.4.

4 Results

4.1 Structural Results

We report field data collected from the Tangra Yumco rift (Figure 4), the southernmost extent of which intersects the IYS ~40 km west of the town of Sangsang (Figure 1). TYC is characterized by a series of approximately north-striking (~N30°E-N35°E) high-angle (\sim 45-70°) active normal faults (Figure 5D), exhuming ~1-2 vertical km of granodiorite in rift footwalls (Figure 5F). In northern TYC (north of \sim 30.5°N) and southern TYC (south of \sim 29.5°N), west-dipping faults bounding the east flank of TYC rift constitute the dominant structures, whereas in the central TYC rift (between 29.5°N to 30.5°N) the dominant structures are east-dipping faults bounding the western rift flank. In both northern and southern TYC, hanging wall rocks consisting of Quaternary glacial and alluvial deposits are cut by a sequence of basin-stepping high-angle normal faults (Figure 5E). In the central TYC rift, hanging wall rocks display synthetic graben structures and stepped fault scarps at the surface,

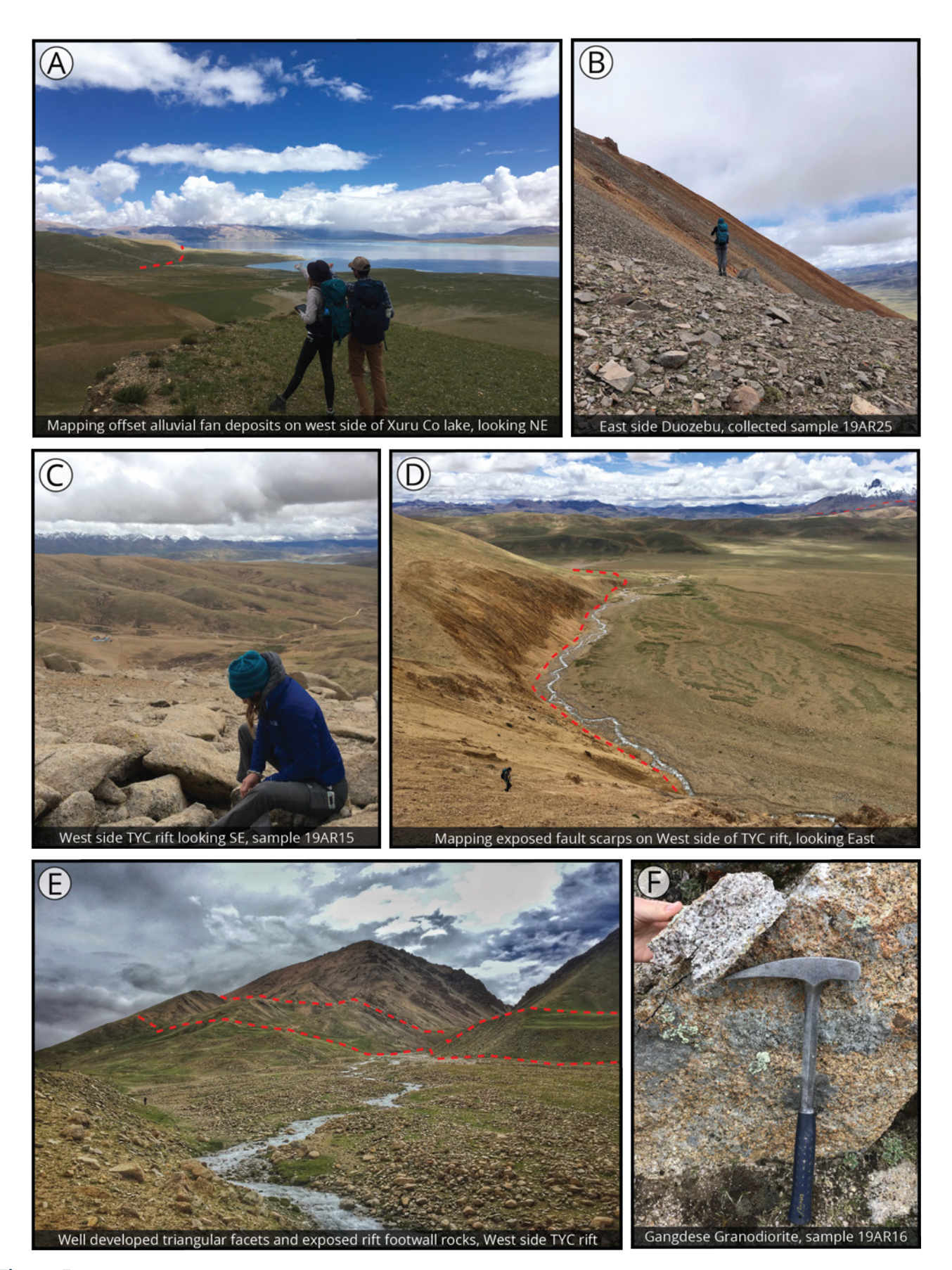


Figure 5 – Field photographs from the southern Tangra Yumco rift. (A) Mapping offset hanging wall alluvial fan deposits west of Xuru Co lake (photo looking NE). Red dashed lines show approximate fault trace. (B) Geologic mapping on the East face of Duozebu at \sim 5,600 m elevation (photo looking NE). (C) Collecting sample 19AR15 from the western footwall of the TYC rift (photo looking SE). **(D)** Mapping along exposed fault scarps, west side TYC. Height of fault scarp exposure is \sim 30 m (\sim 98 ft). (E) Looking SW at the west side of the TYC rift; well-developed triangular facets exposing footwall rocks, sinistral-normal slip causes drainage to be offset towards the NNE. Relief in photo is \sim 777 m (\sim 2,550 ft). **(F)** Gangdese granodiorite sample collected from rift footwall along East side of TYC.

suggesting the occurrence of low-angle detachment style faulting at shallow (\sim 1-2 km) depths (e.g., Axen et al., 1999). Footwall granodiorites display pervasive northeast dipping foliation, with fault plane striations consistent with northeast directed oblique sinistral-normal slip (Figure 4). The general trend of structures mapped from aerial imagery, field measurements, and modern GPS velocities support a preferential NNE-SSW trend of extensional structures at this longitude, suggesting a left-lateral strike-slip component of displacement within TYC and supporting interpretations of a general clockwise rotation of central Tibet (e.g., Zhang et al., 2004; Taylor and Yin, 2009). At the southern extent of the mapped area where TYC intersects the IYS, we observe Xigaze forearc strata faulted onto nonmarine strata of the Kailas Formation along a top-to-the north reverse fault that dips approximately ~75° to the south (Figure 4). Approximately 1.5-2 km to the north, a second top-to-the north reverse fault that dips \sim 64° to the south places rocks of the Kailas Formation in the hanging wall atop Gangdese granites and exhibits fault plane striations consistent with a top-to-the-north-northwest oblique sense of motion. We suggest both structures are splays of the Great Counter Thrust system based on their similar geometries and kinematics (Heim and Gansser, 1975; *Yin et al.*, 1994, 1999a; *Murphy et al.*, 2010).

4.2 Zircon U-Pb Geochronology

Igneous zircon U-Pb results for eighteen samples yield weighted mean ages between \sim 153 Ma and 11 Ma (Figures 6 and 7, Table 1). Fourteen samples yield ages between 58.8 \pm 0.2 Ma and 49.4 \pm 0.2 Ma, consistent with previous results from this region (e.g., Lee et al., 2009; Zhu et al., 2011; Wang et al., 2015), whereas four samples yield ages outside of this range. Sample 19AR11 was collected from a N-S striking \sim 15m-wide porphyritic andesite dike and generated three distinct age domains at \sim 38 Ma (n = 5), 24 Ma (n = 14), and 16 Ma (n = 17) likely due to inheritance, with the highest population of grains yielding a weighted mean age of 16.1 \pm 0.1 Ma (Figure 7; see section 5.1 for further discussion). Samples 19AR25 and 19AR26 are a dark gray porphyritic andesite-to-dacite which intrudes a heavily fractured cataclasite breccia zone along the east face of Duozebu mountain and generated weighted mean ages of 10.9 \pm 0.1 Ma and 11.0 \pm 0.1 Ma, respectively, with sample 19AR26 yielding two age populations at \sim 54 Ma (n = 5) and \sim 11 Ma (n = 17; Figure 7). Finally, sample 19KS34 yields a significantly older weighted mean age of 152.9 \pm 0.6 Ma (Figure 7) and was collected from volcanic rocks just north of Xuru Co lake along a section of the rift where the dominantly N-S striking rift bounding fault curves abruptly to an E-W striking orientation.

Analyzed zircons from this study show oscillatory zonation with no obvious metamorphic rims in CL imagery, widely variable concentrations of U $(\sim 98-5551 \text{ ppm})$ and Th (1055-7438 ppm), and U/Th

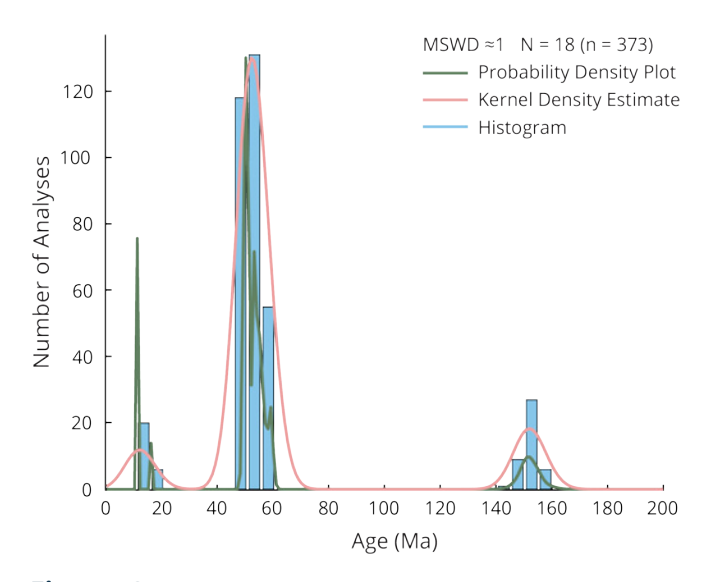


Figure 6 – U-Pb probability density plot (PDP, green), kernel density estimate (KDE, pink), and histogram (blue) for analyses within MSWD \approx 1 (n = 373/698). Grains with >1000 ppm Uranium and ages exceeding 2 σ error are considered outliers and not plotted or included in MSWD calculation.

ratios between 0.33 to 3.49 (Table S2). These results are consistent with an igneous origin (e.g., Corfu et al., 2003; Hoskin and Schaltegger, 2003; Harley et al., 2007; Gehrels et al., 2009). Additionally, no inherited cores were identifiable in CL imagery for all samples other than 19KS34, which revealed oscillatory zoned cores with homogeneous metamorphic rims. Therefore, weighted mean ages for most samples are considered to represent the age of primary zircon crystallization, with the mean age for sample 19KS34 warranting further investigation (see section 5.1). High-U analyses which correlate to anomalously young ages may alternatively indicate Pb-loss (Gehrels et al., 2009), however, zircons in this study show no correlation of high-U concentrations with youngest ages, indicating no analytically significant Pb-loss has occurred. The AgePick tool for Excel (Gehrels, 2009) was utilized to evaluate individual sample analyses and determine outliers based on anomalous age or U concentrations. Analyses for spots recording >1000 ppm U or resulting in ages exceeding 2_{\sigma} error were considered outliers and excluded from data visualizations and interpretation. Sample coordinates and complete data for all U-Pb analyses included in Table S2 (Reynolds, 2023).

Zircon (U-Th)/He Thermochronology

Here we report ZHe mean ages (Figure 8, Figure 9, Figure S3, Table 1, Table S3) for forty-nine samples including thirty-two samples from the southern TYC rift and seventeen samples from three Gangdese rifts (GR) located \sim 90 km (GR1, five samples), \sim 75 km (GR2, ten samples), and \sim 40 km (GR3, two samples) east of TYC. Mean ages and errors were calculated by averaging five single-grain analyses per sample (245 total single grain ages), excluding eight grains that were considered outliers. Outliers were

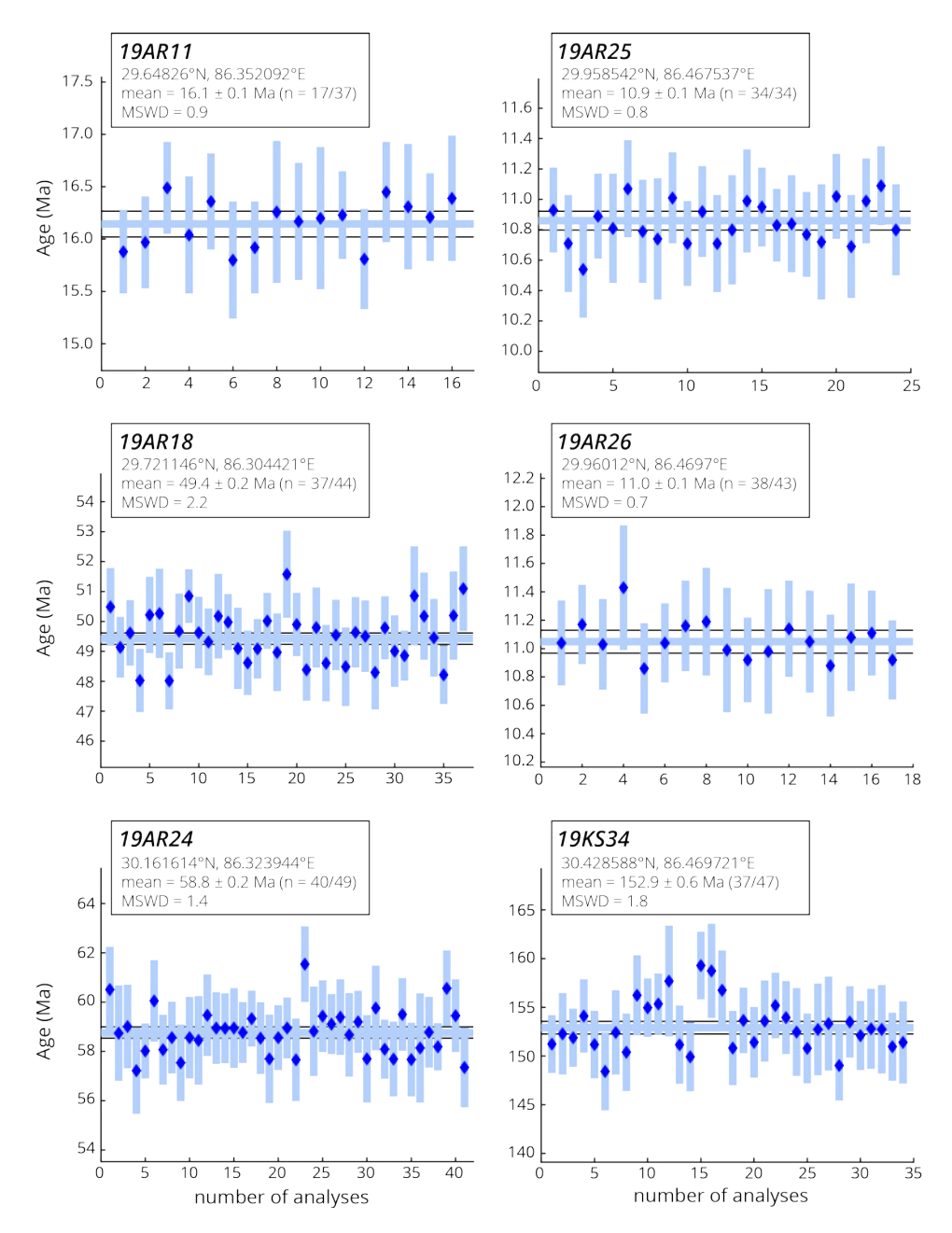


Figure 7 – Igneous zircon U-Pb weighted mean age plots for samples collected from TYC and Gangdese (19AR04, 19AR07, 19AR08) rift footwalls. Ages reflect the timing of latest crystallization with plots for samples 19AR11, 19AR25, and 19AR26 representing youngest age populations (Figure 6). Grains with >1000 ppm Uranium and ages outside of 2σ error were considered outliers and not plotted or included in MSWD calculations. Sample locations shown on geologic map (Figure 4). Weighted mean plots for all samples are included in supplementary Figure S2.

not plotted or included in calculations due to their anomalous results for age, Th/U ratio, or Zr content (Table S3). We note nine samples from TYC (19AR14, 19AR19, 19AR20, 19AR21, 19KS32, 19AL09, 19AL10, 19AL13, 19AL14) and two samples from Gangdese rifts (19AR01 and 19AR06) show poor intra-sample reproducibility (i.e., single-grain ages within each sample yield standard deviations >5 Ma). We report mean ages for these samples for completeness and consider causes of intra-sample age variability in our discussion. Detailed sample data and ZHe results are included in Table S3 (*Reynolds*, 2023).

4.3.1 Tangra Yumco Rift

One hundred sixty single-grain ZHe analyses from southern TYC produced mean ages between 59.3 \pm 0.8 Ma and 4.72 \pm 0.06 Ma (Figure 9, Table 1). Mean ages show no significant correlation with elevation (Figure 8a), grain radius, or effective uranium (eU = [U] + 0.235[Th]; supplementary Figure S3) but correlate with sample latitude (Figure 8b). lack of correlation between age and elevation is illustrated in various sample transects. For example, samples 19AR22, 19AR23, and 19AR24 cover a vertical distance of \sim 250 m yet the sample in the center (19AR23; 24.6 \pm 0.3 Ma) is 15-20 Myr older than the lower and upper samples. pattern can be seen at other sampling locations

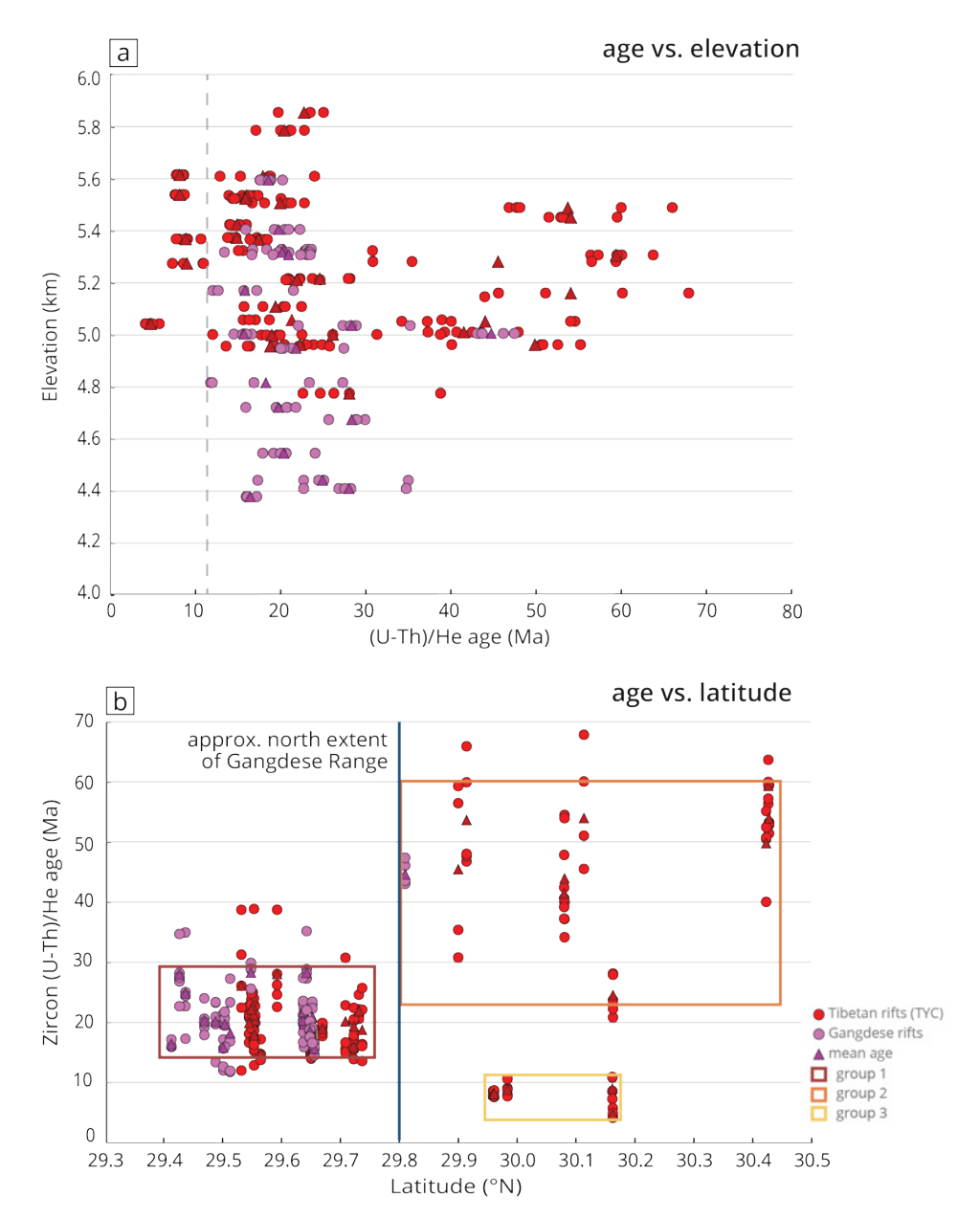


Figure 8 - (a) ZHe age plotted against elevation; triangles are mean ages for each sample. Colors differentiate samples collected from the TYC rift (red) and Gangdese rifts (pink). Samples show no correlation between age and elevation. Note samples younger than ~12 Ma (gray dashed line) produce well constrained ages suggesting rapid exhumation, whereas samples older than \sim 12 Ma show broader intra-sample age variability. (b) ZHe age as a function of sample latitude. Samples from both TYC and Gangdese rifts that were collected at Gangdese latitudes (group 1, red box) exhibit mean ages clustered primarily between ~22-15 Ma, whereas samples north of and proximal to the northern extent of the Gangdese Range $(\sim 29.8^{\circ}\text{N}, \text{blue line})$ exhibit both older Paleocene to Eocene $(\sim 59-45 \text{ Ma})$ ages (group 2, orange box) and younger late Miocene to Pliocene (~9-4 Ma) mean ages (group 3, yellow box). The wide intra-sample age variability for individual samples in group 2 may indicate a greater length of time spent at depth in the ZHe partial retention zone.

(e.g., 19AR15) where samples were collected at short vertical distances from each other (e.g., Figure 8a). Samples from the TYC rift plotted against latitude can be separated into three groups (Figure 8b) by mean age: Group one (red box) includes samples collected from latitudes where the TYC rift crosscuts the Gangdese Range (~29.4°N-29.8°N) and is comprised of Oligocene to mid-Miocene ages (\sim 28-15 Ma). Group two (orange box) and group three (yellow box) include samples from latitudes north of the Gangdese Range (~29.8°N-30.43°N) and yield Paleocene-Eocene (~59-41 Ma) and late Miocene-Pliocene (\sim 9-4 Ma) ages, respectively.

Group one: the nineteen samples in group one yield mean ages between ca. 28-15 Ma, with all but three samples (19AR21, 19AR23, 19AL09) having mean ages falling within the narrower window of \sim 23-16 Ma. Sample 19AR21 was collected from the mid-rift pluton near the southern end of TYC and yields widespread single-grain ages between 38.74 \pm 0.49 Ma and 22.57 \pm 0.29 Ma (mean age of 28.04 ± 0.36 Ma). Sample 19AL09 was collected from the southeast flank of the TYC rift proximal to the mapped location of two thrust faults and the Kailas Conglomerate (Figure 4), yielding widespread single-grain ages between 38.71 \pm 0.51 Ma and 12.00

 \pm 0.17 Ma (mean age of 26.10 \pm 0.34 Ma). Sample 19AR23 was the only sample in the group one age range that was collected north of Gangdese Range latitudes (~30.16°N) and yielded single-grain ages between 28.11 \pm 0.36 Ma and 20.85 \pm 0.28 Ma with a mean age of 24.56 \pm 0.31 Ma. Age-elevation relationships for sample transects suggest complex cooling histories, with some samples generating well constrained intra-sample age ranges spanning as little as \sim 1.98 Myr, whereas others span as much as \sim 26.7 Myr within a single sample.

Group two: eight samples including 19AR19, 19AR20, 19KS32, 19KS33, 19KS34, 19AL12, 13AL13, and 19AL14 yielded mean ages between ∼59.3-45.5 Ma. Samples 19AR19 and 19AR20 were collected from two ~6 m tall east facing fault scarps located \sim 5-7 km southeast of Duozebu (Figure 4). Samples 19AL12-14 were collected \sim 15 km and \sim 10 km southwest of Xuru Co lake along the western flank of TYC. Finally, 19KS32-34 constitute the farthest north transect in this study and were collected ~5 km northeast of Xuru Co lake where the normal fault bounding the west flank of TYC bends abruptly from approximately N-S striking to E-W striking. Each of these samples produced significantly older mean ages than Group one samples and widespread intra-sample age variability. Age-elevation relationships for sample transects suggest prolonged cooling histories, with all samples producing broad intra-sample age ranges spanning more than 8 Myr and up to 28.5 Myr.

Group three: five samples including 19AR22, 19AR24, 19AR25, 19AR26, and 19AR27 yielded mean ages falling between ~9.0-4.7 Ma. Samples 19AR22 and 19AR24 were collected along a footwall transect from the west side of TYC just southwest of Xuru Co lake and yield mean ages of 4.72 \pm 0.06 Ma and 8.98 \pm 0.12 Ma. It is noteworthy that sample 19AR22 which produced the youngest mean age of all samples was collected from exposed footwall granodiorite along an apparently active basin-bounding normal fault. We observed biotite chloritization within the sample that could potentially be related to hydrothermal alteration. Samples 19AR25-27 were collected from the east and north faces of Duozebu and yield well-constrained single-grain ages between 10.62 \pm 0.13 Ma and 7.58 \pm 0.09 Ma and mean ages of 8.11 \pm 0.10 Ma, 8.13 \pm 0.10 Ma, and 8.83 \pm 0.11 Ma, respectively. We note the possibility that samples 19AR25-27 could simply reflect cooling subsequent to emplacement of syn-extensional igneous deposits at Duozebu and further discuss these samples in section 5.1. With the exclusion of sample 19AR23 (mean age of 24.56 \pm 0.31 Ma) from sample transect 19AR22-24, age-elevation relationships for sample transects in group three suggest rapid exhumation and cooling, with all samples producing well constrained intra-sample age ranges less than \sim 3.7 Myr.

4.3.2 Gangdese Rifts

Eighty-five single-grain ZHe analyses were completed for seventeen samples from three Gangdese rifts located \sim 90 km (GR1, five samples), \sim 75 km (GR2, ten samples), and \sim 40 km (GR3, two samples) east of TYC. Gangdese rift samples yield mean ages between 27.98 \pm 0.35 Ma and 15.65 \pm 0.2 Ma (Figure 8, Figure 9, Table 1, Table S3). Mean ages show no clearly meaningful correlation with sample elevation, grain radius, or effective uranium (Figure 8a; Table One north-south oriented transect of five samples was collected along GR1 including 19AR04, 19AR05, 19AR06, 19AR07, and 19AR08 from south to north. Nine samples along three approximately east-west transects were collected from the east flank of GR2 including 19AR01, 19AR02, 19AR03, 19GR01, 19GR02, 19GR03, 19GR05, 19GR06, and 19GR07. One sample, 19AL20, was collected from the northwest flank of GR2. Finally, samples 19AL15 and 19AL18 were collected along a north-south transect in GR3.

Of the seventeen Gangdese rift samples, all except one sample (19AL20) yield Oligocene-early Miocene mean ages between \sim 28-15 Ma and twelve of them fall within the narrower age range of \sim 23-16 Ma (Figure 8a). These ages align with group one samples from the TYC rift collected at latitudes where TYC crosscuts the Gangdese Range. Samples 19AR05 and 19AR06 of this group were collected from granodiorites near the fault contact with the basal Kailas Formation and yield the oldest mean ages of 27.98 \pm 0.35 and 24.87 \pm 0.32, respectively. Sample 19AL20 was the farthest north Gangdese rift sample, collected near the northern extent of the Gangdese Range, and yields an older Paleocene-Eocene mean age of 44.68 \pm 0.53, aligning with group two ages for samples from the TYC rift. Age-elevation relationships for sample transects suggest monotonic cooling for some samples and complex cooling histories for others, with some Gangdese rift samples generating well constrained intra-sample age ranges spanning as little as \sim 1.23 Myr, whereas others span up to \sim 17.7 Myr within a single sample. Sample transects suggest average exhumation rates of \sim 0.1 mm/yr for GR1 and \sim 0.2 mm/yr for GR2.

When comparing the ages of samples from the Gangdese rifts (Figure 8b, pink) and TYC rift (Figure 8b, red), we observe that all portions of the rifts overlapping the Gangdese Range (\sim 29.4-29.8°N) produce similar mean ages (group one), whereas samples collected from the portions of rifts extending north of the Gangdese Range or proximal to its northern extent (19AL20) yield either older (group 2) or younger (group 3) mean ages. interpretations related to this observation are discussed in detail in section 5.1.

4.4 HeFTy Thermal Model Inputs and

HeFTy inverse modeling for each of eighteen samples from southern TYC was completed using input parameters for the median grain from each sample (i.e., single-grain models for each sample). Model inputs include the uncorrected age and corresponding error, grain radius, and measured concentrations of U and Th for each grain. Model calibrations from Guenthner et al. (2013) for zircon and helium diffusion kinetics and stopping distances from Ketcham et al. (2011) were selected. following criteria were used to define the searchable space for t-T paths during model runs:

- 1. Paths for samples with no U-Pb results began above ZHe closure temperature (>200 °C) with initial timing left unconstrained (100-0 Ma) to allow broad exploration of the t-T space.
- 2. Zircon U-Pb weighted mean ages indicate temperatures >900 °C from \sim 59-49 Ma.
- 3. ZHe ages reflect cooling through 200-140 °C from \sim 60-4 Ma. Note that model inputs for individual grains force t-T paths to pass through a specified point as defined by the ZHe model.
- 4. Paths end at the model surface (20-0 °C) at present day (0 Ma).

The t-T histories resolved by HeFTy are shown as a series of good (pink) and acceptable (green) t-T paths and a single best-fit path (black) from n = 50,000 model runs (Figure 10). To determine spatial trends in HeFTy predicted thermal histories, the most obvious distinctions are observed when comparing the farthest south and farthest north samples that have been reset. Looking at trends and clusters within the t-T paths in Figure 10, each sample likely experienced a multi-phase cooling history, with a likely initial phase of slower cooling followed by one or more phases of rapid cooling. The onset of rapid cooling in the southern-most sample (19AL06) occured by \sim 22 Ma, whereas in the northern-most sample (19AR24) the onset of rapid cooling is much younger, falling between \sim 12 and 8 Ma (Figure 10). These results support observations that the onset of rapid cooling youngs to the north, which broadly agrees with the ZHe results from this and previous studies (e.g., Styron et al., 2015).

Discussion 5

5.1 **Kinematic History of the Tangra** Yumco Rift

Structural results from TYC indicating north-northeast directed oblique sinistral normal slip are consistent with field observations from previous studies in the northern (Wolff et al., 2019) and southern (Wolff et al., 2023) TYC rift, and broader plateau-scale observations of Tibetan rift orientation and kinematics (e.g., Kapp and Guynn, 2004). Near the

southern extent of the TYC rift, we observe Xigaze forearc strata faulted onto the Kailas Formation, and Kailas Formation strata faulted onto rocks of the Gangdese batholith along two south-dipping, top-to-the north reverse faults (Figure 4). The faults dip \sim 64-75° to the south and exhibit slickenlines consistent with top-to-the-northeast oblique sense of motion. We interpret these faults as splays of the GCT, as their geometry and kinematics are consistent with regional interpretations and recent work from the Dajiamang Tso rift which crosscuts the IYS just 50 km west of TYC (Burke et al., 2021). The northern and southern TYC are bounded by dominantly high-angle normal faults with minimal surficial evidence for low-angle faulting (after Wolff et al., 2019, 2023). This observation may be consistent with fault models for other Tibetan rifts suggesting high angle normal faults are likely to sole into a master rift-bounding fault at depth (e.g., Kapp et al., 2008). Additionally, similarities of the southern TYC rift to the Lunggar and Yadong Gulu rifts include the abandonment of rift bounding structures in favor of slip along a basinward-stepping series of high-angle normal faults, and the apparent presence of a young (ca. 8 Ma) intra-basin topographic high (Duozebu, \sim 6,429m).

The oldest igneous U-Pb mean age in this study from sample 19KS34 (152.9 \pm 0.6 Ma) comes from a hornblende- and biotite-poor, pink-white granite collected just north of Xuru Co lake where the main fault bounding the west side of the TYC rift curves sharply from a N-S strike orientation along the western shore of Xuru Co lake to a nearly E-W oriented fault strike along the north shore of the lake. We interpret this age to reflect rare but previously documented igneous rock crystallization at \sim 150 Ma within 0-150 km distances from the IYS, likely related to Gangdese Range magmatism which was active from at least ca. 150-40 Ma (Lee et al., 2009), though we note significantly higher abundances of ages between ca. 140-120 Ma are typically reported for the northern Lhasa terrane (e.g., Orme et al., 2015). The early-Miocene U-Pb weighted mean age for sample 19AR11 (16.1 \pm 0.1 Ma), and middle to late-Miocene U-Pb weighted mean ages for samples 19AR25 and 19AR26 (10.9 \pm 0.1 Ma and 11.0 \pm 0.1 Ma) are likely related to their collection from syn-extensional igneous deposits. Sample 19AR11 is from a \sim 15-m-wide E-W opening porphyritic andesite dike yielding three age domains, potentially due to inheritance or incorporation of older zircon crystals from the host rock. Samples 19AR25 and 19AR26 were collected from the east face of Duozebu, a prominent intra-basin high (>6,500 m) within the central portion of the southern TYC rift. Sample 19AR25 was collected from a dark gray, porphyritic andesite to dacite intruding a cataclasite breccia, and sample 19AR26 was collected from a phaneritic diorite deposit just \sim 0.3 km northeast of sample 19AR25. U-Pb results for the E-W opening synextensional dike (19AR11, \sim 16.1 \pm 0.1 Ma) are

consistent (\pm 2 Ma) with dating of extensional dikes near the Daggyai Tso graben (~18 Ma, Williams et al., 2001) located ~75 km west of sample 19AR11, as well as biotite 40Ar/39Ar age estimates from the Lopu Kangri rift (~16 Ma, Sanchez et al., 2013; Laskowski et al., 2017) and Thakkhola graben (\sim 14 Ma, Murphy et al., 2010) that have been used to infer a minimum age of east-west extension onset in southern Tibet (e.g., Yin and Harrison, 2000; Burke et al., 2021). Therefore, we interpret the age of 16.1 \pm 0.1 Ma to support a minimum age of onset for E-W extension in southern TYC, with continued and likely rapid rift exhumation through \sim 11 Ma reflected by crystallization of syn-extensional intrusive igneous bodies in southern TYC.

Results from ZHe dating show a clear correlation between age and sample latitude (Figures 8b, 9). ZHe mean ages for all samples from Gangdese latitudes in the southern map area, regardless of their collection from the TYC rift or Gangdese rifts, fall between \sim 28-16 Ma and cluster around \sim 21 Ma, whereas samples north of the Gangdese Range produced both younger (13-4 Ma) and older (66-45 Ma) ages. We interpret Oligocene to early-Miocene ZHe ages from Gangdese latitudes as reflecting a distinct exhumation event prior to TYC rift initiation, mid-Miocene to Pliocene ZHe ages to reflect samples that have been reset due to rift-related exhumation and their position in the TYC rift and consistency with rift timing estimates from previous studies, and Paleocene-Eocene ZHe ages to reflect partially reset samples from portions of the TYC rift that have experienced insufficient rift exhumation for samples to be fully reset (Figures 4 and 9). We interpret the Paleocene-Eocene ZHe ages as partially reset due to their wide intra-sample age variabilities suggesting a protracted cooling history or in other words, a longer period of time spent within the partial retention zone of the ZHe system. Observed widespread intra-sample ages variability in these samples could be explained by structural controls related to sample location, with some samples collected along minor fault scarps or E-W striking portions of major fault scarps. Samples 19KS32-34 were collected in a portion of TYC where the main rift bounding fault curves from a N-S strike orientation to nearly E-W orientation and may be a region where slip is preferentially dominated by strike-slip rather than dip-slip motion. Samples 19AR19 and 19AR20 were collected form portions of the rift where fault segments are relatively young, small, and do not appear to be linked with one another, potentially causing greater partitioning of E-W extensional deformation across multiple fault segments and leading to less extension than in areas of TYC where E-W extension is concentrated along more well-developed, longer, and more interconnected fault segments. Individual samples exhibiting a large spread or variability in ZHe age may indicate a longer period of time spent in the ZHe PRZ due to slower cooling and exhumation rates along these

fault segments.

Based on kinematic observations from the field, normal fault patterns from geologic mapping, U-Pb weighted mean ages, and spatial trends in ZHe ages from this and previous studies, we interpret the best fit kinematic model for the TYC rift to be the segment linkage model. This model predicts similar patterns of fault displacement to what is observed in TYC, with the overlapping nature of numerous normal faults in the central TYC rift (Figure 4) suggesting initiation as segments prior to coalescence into larger cohesive structures. The fault traces in the study area are moderately sinuous (Figure 4), potentially reflecting the locations where previously isolated segments began to overlap and merge (e.g., Curry et al., 2016). Additionally, the complex distributions in the age of extension onset along strike of TYC are potentially related to variations in the timing and magnitudes of exhumation along different fault segments (i.e., some segments with greater offset generate enough exhumation to reset ZHe sample ages while other fault segments do not). An earlier onset of extension, higher magnitudes of extension, and greater exhumation rates in the southern portion of the TYC rift could be attributed to most E-W extension being accommodated along a larger fault consisting of linked fault segments rather than E-W extension being partitioned across several smaller or un-linked fault segments, which may be operating in the central and northern portions of the TYC rift. Additionally, the timing of onset for rapid exhumation due to faulting is variable across sample transects from southern TYC, which may also be best explained by the segment linkage fault growth model. An alternate explanation is that the faults bounding the TYC rift may have evolved due to some force causing the overall fault displacement to increase in rate and magnitude from south to north. However, this south to north sweep is not explicitly necessary to explain our results, as variability in the timing and rates of exhumation and partitioning of slip across multiple fault segments could explain this independently. Thermal history models reveal multi-stage cooling histories for footwall rocks in southern TYC, with the timing of rapid exhumation for each sample indicated by the break in slope. The t-T paths for the farthest south reset sample (19AL06) indicate rapid exhumation beginning at around ~18 Ma, consistent with the minimum age for extension onset of \sim 16 Ma given by U-Pb dating of an extensional dike in the southern TYC, whereas the model for the farthest north reset sample (19AR24) indicates rapid exhumation at around \sim 8 Ma. If models for samples between 19AL06 and 19AR24 indicate a smooth northward sweep in the onset of rapid exhumation, then perhaps there is a major tectonic influence on the northward propagation of accelerated rifting during mid-Miocene to Pliocene time. If the models indicate inconsistencies or irregularities in the onset of rapid exhumation from south to north, then it is likely the segment linkage model better explains

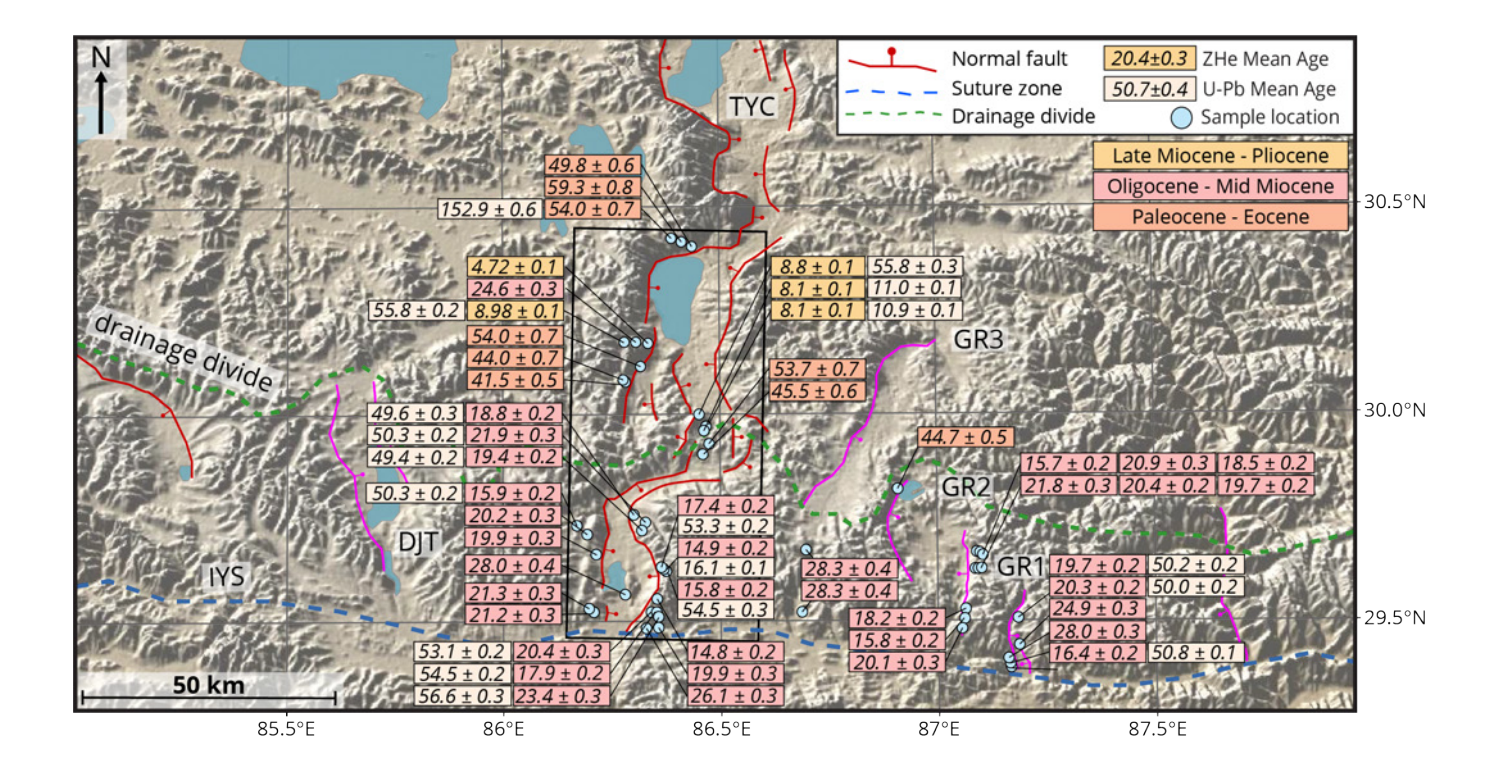


Figure 9 – Digital elevation model of the southern TYC rift showing 49 ZHe mean ages and 18 U-Pb weighted mean ages for samples from the TYC rift and nearby Gangdese rifts (GR1, GR2, GR3) which crosscut the high topography of the Gangdese Range. ZHe ages are color coded: orange = Paleocene to Eocene; red = Oligocene to mid-Miocene; yellow = late Miocene to Pliocene. The black box shows the extent of geologic mapping (Figure 4). The green dashed line shows the approximate location of the Gangdese drainage divide. Blue dashed lines indicate suture zones; IYS = Indus-Yarlung suture. DJT = Daijaimang Tso rift. Normal fault traces from geologic mapping and HimaTibet database (Styron et al., 2010). Topography from GeoMapApp (VE = 4).

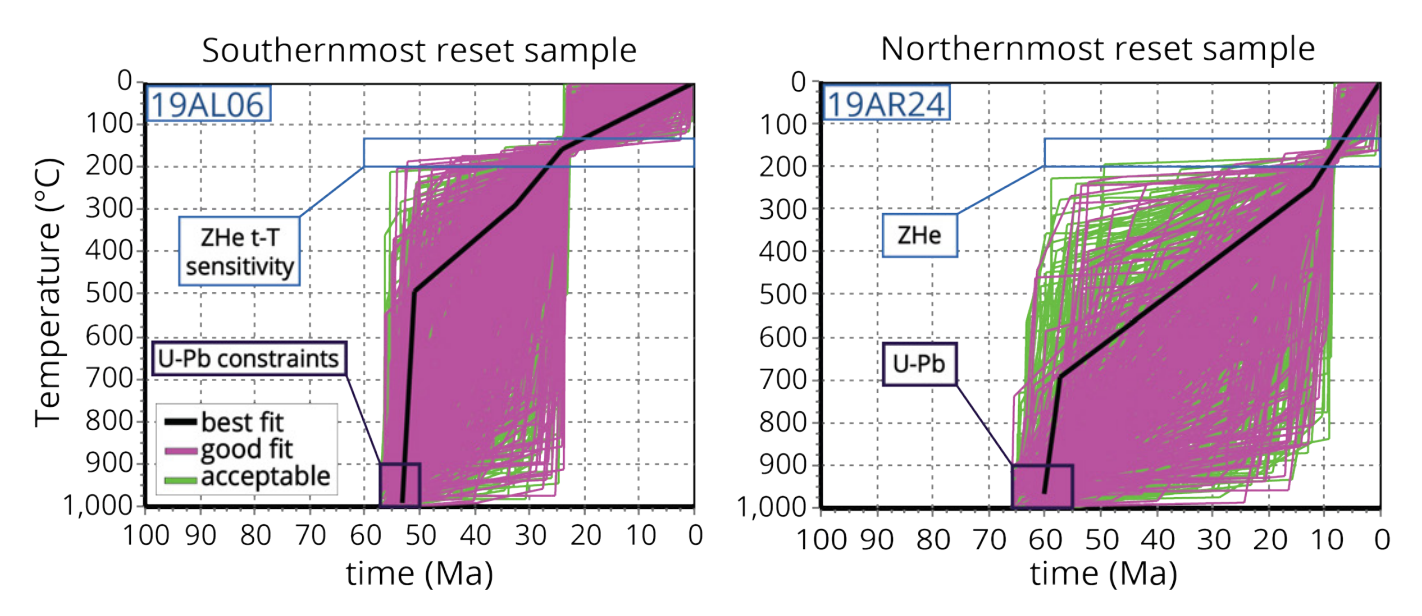


Figure 10 - HeFTy models for the southern-most and northern-most reset samples from the TYC rift showing best fit (black), good fit (pink), and acceptable fit (green) paths. Model paths (n= 50,000) initiate within the dark blue boxes representing time-Temperature constraints from U-Pb dating of samples 19AL06 (>900°C between 58-50 Ma) and 19AR24 (>900°C between 65-55 Ma). Paths end at the surface (20-0°C) at present day (0 Ma) and are dominantly constrained by ZHe t-T sensitivities (light blue boxes) that are established through model inputs including the age and diffusion parameters (e.g., grain radius) specific to the median grain for each sample. Thus, the light blue boxes are a visual representation of model input parameters rather than an additional constraint box in the model space. ZHe HeFTy model results for all samples are available in supplementary Figure S4.

the observed spatial variations in the onset of rapid exhumation.

5.2 Exhumation History of South-Central Tibet

5.2.1 Post-Collisional Deformation Along the Gangdese Range and Great Counter Thrust

ZHe ages from latitudes where the TYC rift crosscuts the Gangdese Range (group one) generated mean cooling ages between ca. 28-15 Ma, with twelve of the seventeen Gangdese rift samples and sixteen of the nineteen TYC rift samples falling within the narrower mean age range of ca. 23-15 Ma (Figure 8). These ages are older than samples interpreted as reset rift footwall samples north of the Gangdese Range, suggesting a different structural mechanism for their cooling. The oldest mean age in group one (28.04 \pm 0.36 Ma) from sample 19AR21 was calculated from relatively widespread single-grain ages from 22.57 \pm 0.29 Ma to 38.74 \pm 0.49 Ma. The widespread single-grain ages from this and other samples overlapping the Gangdese Range largely predate even the earliest estimates for extension onset in southern Tibet from prior studies and could alternatively reflect exhumation resulting from rock uplift in the hanging wall of contractional structures in this region that are proposed to have been active by ~27 Ma (Yin et al., 1994; Laskowski We note that samples positioned et al., 2018). in the footwall of the TYC rift have likely also experienced exhumation due to normal faulting and erosion during the mid-Miocene-Pliocene. A combination of exhumation due to thrusting, erosion and normal faulting could possibly explain some of the widespread intra-sample ZHe ages between \sim 28– 12 Ma for TYC rift samples overlapping the Gangdese Range. Sample 19AR21 was collected from the mid-rift pluton at the southern end of TYC (Figure 4). With a mean age of \sim 28 Ma, it is possible the mid-rift pluton is a portion of the Gangdese Range which became isolated within the basin as the TYC rift crosscut and dissected the Gangdese Range during Miocene time. Conversely, the young late Miocene ages from the east and north faces of Duozebu likely reflect rift exhumation at \sim 11 Ma, suggesting Duozebu represents a rift-related intra-basin high rather than an isolated portion of the Gangdese Range, similar to documented intra-basin highs in other Tibetan rifts (e.g., central Lunggar rift, Kapp et al., 2008). The southernmost sample transect from TYC (19AL06, 19AL07, 19AL08) also produced ZHe mean cooling ages between ca. 23-18 Ma, consistent with previous estimates for the timing of activity along the south-dipping Great Counter Thrust beginning as early as 23 Ma and continuing until ca. 18-13 Ma (Laskowski et al., 2018; Kapp and DeCelles, This range of ZHe ages overlaps timing estimates for deposition of the Kailas Formation in south-central Tibet beginning at ca. 21 Ma (DeCelles et al., 2011; Leary et al., 2016) and subsequent

exhumation of the IYS and Kailas Formation at ca. 19-15 Ma (*Carrapa et al.*, 2014). The timing of exhumation of the Indus-Yarlung Suture zone and Kailas Formation could be related to focused erosion along the GCT, Yarlung River establishment, and drainage reorganizations documented in the early Miocene (Carrapa et al., 2014; Lang and Huntington, 2014). Therefore, we interpret that the Gangdese Range has experienced at least semi-continuous exhumation during the time in which it has been construed as located in the hanging wall of the GT (Yin et al., 1994), in the footwall of the GCT, and/or in the hanging wall of a north-dipping normal fault which possibly created accommodation space for deposition of the Kailas Formation (DeCelles et al., 2011; Wang et al., 2015; Leary et al., 2016; Laskowski et al., 2018).

5.2.2 Timing of Exhumation and Cooling Along Tibetan Rifts and Gangdese Rifts

Potential differences in the structural style, timing, and rates of extension between Tibetan rifts and Gangdese rifts have been investigated by few studies (*Yin*, 2000; *Burke et al.*, 2021). Here we compare kinematic interpretations based on field observations and thermochronologic data from the TYC rift with results from three nearby Gangdese rifts (GR1, GR2, and GR3). Through the comparison of Tibetan rifts and Gangdese rifts, we investigate the potential for a shared mechanism of origin as opposed to rift initiation related to discrete structural processes or tectonic events. Additionally, we establish potential links between rifting and the evolution of the Gangdese drainage divide. Samples from TYC which reflect rift-related exhumation and cooling rather than pre-extensional cooling include those from latitudes north of the northern extent of the Gangdese Range (\sim 29.8°, Figure 8b) consisting of ZHe cooling ages in Group two (\sim 59-45 Ma, 8 samples) and Group three (\sim 9-4 Ma, 5 samples). Group two is comprised of Paleocene-Eocene ages which likely reflect un-reset or partially reset samples collected from fault segments that have experienced lesser magnitudes of extension due to structural controls, whereas Group three contains late Miocene-Pliocene ages that are interpreted to reflect the timing of recent rift-related exhumation in the southern TYC rift between 9-4 Ma (see section 5.1, Figures 4 and 9). We interpret E-W extension in the southern TYC rift to have initiated by \sim 16 Ma continuing until at least 4 Ma, whereas E-W extension across the Gangdese rifts appears to have begun by \sim 28 Ma and continued until \sim 16 Ma.

Previous studies document spatiotemporal trends of ZHe ages indicating an older in the south and younger in the north timing of extension onset, with thermal models indicating multi-stage cooling histories with a northward younging acceleration of extension rates along the TYC rift during late Miocene to Pliocene time (~13-5 Ma; Wolff et al., 2019). This

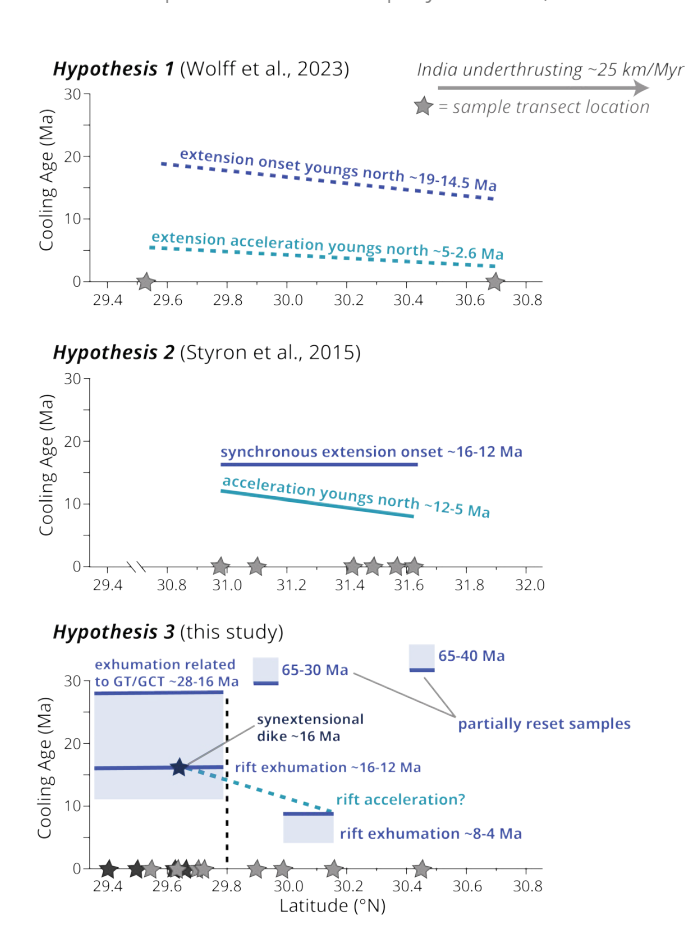


Figure 11 – Tectonic hypotheses for extension in southern Tibet. Each hypothesis shows cooling age versus latitude to evaluate along-strike trends. Stars on x-axis represent In hypothesis 1 after Wolff et al. sample transects. (2023), both the timing of extension onset and rift acceleration in TYC young to the north at a rate which is consistent with underthrusting of the Indian plate (~25 mm/yr). Hypothesis 2 after the work of Styron et al. (2015) in the Lunggar rift presumes synchronous extension onset followed by a northward sweeping acceleration of extension rates. This study proposes hypothesis 3 as the best fit model based on ZHe results from this study, relating the timing of exhumation at Gangdese latitudes to contraction and uplift along the GT and/or GCT constrained by extensional dikes from this (16.1 \pm 0.1 Ma) and other studies, potentially reflecting a minimum age of onset for E-W extension in southern TYC, whereas samples north of the Gangdese Range reflect the rift exhumation signal and reveal the timing of extension onset in south TYC. Each tectonic model is consistent with India underthrusting as a driver of extension but reflective of different kinematic models. Hypothesis 1 is most consistent with model (b) tectonically influenced tip propagation, hypothesis 2 which predicts synchronous extension onset is most consistent with model (d) constant length. Based on our data for hypothesis 3, we interpret model (c) fault segment linkage as the best fit kinematic model for south TYC due to the observed variability in the age of extension onset along-strike, with this model also predicting similar map patterns of fault displacement to structural observations from South TYC.

observed south to north acceleration of exhumation rates through time has been previously attributed to the northward propagation of underthrusting Indian lithosphere beneath south-central Tibet (DeCelles

et al., 2002; Kapp and Guynn, 2004; Styron et al., 2015; Wolff et al., 2019, 2023). However, we document significantly more complex spatial relationships for the timing of exhumation in southern TYC (Figure 11), which could alternatively reflect variable timing, rates, and magnitudes of extension along different This may also relate to field fault segments. observations and mapping results revealing greater horizontal displacement in the central TYC rift rather than northern or southern TYC, which may reflect a complex zone of interaction and linkage between fault segments. Furthermore, the presence of both high- and low-angle extensional structures across Tibet and their variabilities in fault length, magnitude, and strike orientation are suggestive of spatial variability in the mechanical and/or thermal properties of Tibetan lithosphere (e.g., Wolff et al., 2019; Bischoff and Flesch, 2018), or alternatively, that the stress field produced by oblique collision of India with Asia exerts a key control on Tibetan rift structure and kinematics (Kapp and Guynn, 2004). Advanced comparisons of rift kinematics across the Plateau and between Tibetan and Gangdese rifts may help discern which of these factors is likely to exert the most influence or control on the variable expression of continental rifting across the Plateau.

Based on distinctions in the timing of rift initiation, rates and magnitudes of extension, and fault growth model interpretations, we suggest the Gangdese rifts and Tibetan rifts initiated and evolved in response to distinct tectonic events or structural controls. For sample transects from Gangdese rifts, the timing of exhumation is nearly coeval along all three sample transects from GR2 within the resolution of the thermochronology data. Our interpretation is that the Gangdese rift data are more closely aligned with the constant fault-length kinematic model. This model, although represented as a distinct end member, may be the most accurate within the spatial scale of this study as rifting in the Gangdese Range beginning at \sim 28 Ma and continuing until \sim 16 Ma could relate to the timing of exhumation during Gangdese Range uplift, with continued exhumation along Gangdese rifts simply balancing continued uplift of the Gangdese Range (e.g., Sundell et al., 2021). The Gangdese rifts likely initiated at similar to present-day lengths due to a "block" uplift of the entire Gangdese Range and accumulated near present-day magnitudes of extension by ca. Ma, in broad agreement with previous studies investigating the timing and structural morphology of Gangdese rifts (Burke et al., 2021). It is likely that minimal additional rift exhumation has occurred or is driven by subsequent tectonic processes like India underthrusting which has been interpreted as a driving force for northward sweeping accelerated extension in Tibetan rifts.

5.2.3 Implications for the Dynamics of **East-West Extension in Southern Tibet**

Many models have been proposed to explain the dynamics or driving forces of extension in Tibet, with each model characterized by testable predictions for the spatial and temporal distributions of the age of extension onset, rates and magnitudes of extension, fault orientations, and relation to magmatism. Here we compare our data and observations from TYC and Gangdese rifts to predictions from four classic dynamic models: (a) removal of dense lithosphere, (b) lithospheric weakening, (c) decreasing horizontal collisional stress, and (d) increasing crustal thickness by underthrusting India (Figure 12).

The results of this study suggest predictions of models (a), (b), and (c) cannot fully explain the observed spatial pattern and timing of rifting in southern Tibet, consistent with interpretations from previous studies which support the India underthrusting model as the best-fit dynamic model for Tangra Yumco and other rifts (Styron et al., 2015; Wolff et al., 2019, 2023). In this model, underthrusting of Indian lithosphere beneath Tibet thickens the crust to reach a critical gravitational potential energy (GPE), causing the maximum principal stress (σ 1) to rotate from horizontal to vertical and initiating E-W extension in southern Tibet (e.g., Yin, 2000; DeCelles et al., 2002; Kind et al., 2002; Tilmann et al., 2003; Kapp and Guynn, 2004; Styron et al., 2011, 2013, 2015; Sundell et al., 2013, 2021; Wolff et al., 2019, 2023). This model was initially suggested to follow synchronous extension onset across southern Tibet in middle to late-Miocene time due to a gravitational collapse of the thickened Plateau (Styron et al., 2015). However, this interpretation is inconsistent with later studies that show rifting began earlier and was diachronous across Tibet, with most graben systems initiating between 16 and 8 Ma (e.g., Laskowski et al., 2017; Wolff et al., 2019, 2023; Burke et al., 2021; Bian et al., 2022). Regardless of variabilities in the timing of extension onset, previous studies supporting the India underthrusting model find initially low rates and magnitudes of extension (\sim 1 mm/yr), followed by a northward sweeping acceleration of extension rates (~1.5-5 mm/yr) during the late Miocene-Pliocene (∼12-5 Ma) tracking the leading edge of underthrusting Indian lithosphere which also cannot be explained by the other models (e.g., Styron et al., 2015; Wolff et al., 2023). Active rifting can be explained by the continued insertion of Indian crust beneath Tibet which further increases Plateau crustal thickness, driving coeval rifting to balance the GPE of the plateau (e.g., Sundell et al., 2021). Rifts in southern Tibet would experience a longer period of accelerated extension than those in central Tibet and therefore have stronger morphological expressions and greater magnitudes of extension, with normal fault orientations in both southern and northern Tibet following a pattern suggesting their common mechanism of origin (Kapp and Guynn, Finally, documented bimodal volcanism 2004).

(Williams et al., 2004; Zhu et al., 2005, 2012) and seismic studies (e.g., Owens and Zandt, 1997; Nábelek et al., 2009) provide additional supporting evidence for the India underthrusting model independent from reported thermochronologic data.

The 245 ZHe ages produced in this study allow us to further ground-truth dynamic model predictions for the TYC rift. Our results indicate rifting in southern TYC initiated in Miocene time by a minimum of \sim 16 Ma and has continued until at least \sim 4 Ma, with field observations suggesting rifting is active and ongoing (Figure 5). We document complex spatial relationships for the onset of exhumation, with ages at Gangdese Range latitudes likely reflecting a prior cooling history, and ages north of the Gangdese Range suggesting variable timing, rates, and magnitudes of extension across multiple fault segments along the TYC rift (Figure 8). It is unclear whether fault processes such as segment linkage or the stress field produced by oblique collision and underthrusting of India (e.g., Kapp and Guynn, 2004) exert a greater control on our results and thus on Tibetan rift structure, kinematics, and dynamics. Advanced comparisons of rift kinematics and dynamics across the Plateau and between Tibetan and Gangdese rifts through thermal and kinematic modeling may help discern which of these factors is likely to exert the most influence on the expression and evolution of continental rifts across the Plateau.

Development of the Gangdese 5.3 **Drainage Divide**

This study reveals ZHe ages between ca. 28 Ma and ca. 15 Ma for all samples collected at latitudes between \sim 29.4°N-29.8°N, which we interpret to reflect enhanced exhumation (where exhumation = surface uplift – rock uplift; *England and Molnar*, 1990) related to the growth of the Gangdese Range. These ages overlap existing timing estimates for the GT and GCT from ca. 23 Ma continuing as late as 18-13 Ma in this region (Laskowski et al., 2018; Kapp and DeCelles, 2019; Taylor et al., 2021) and timing estimates for deposition of the Kailas Formation between ca. 26-18 Ma across southern Tibet (Leary et al., 2016). The timing of Kailas Formation deposition is hypothesized to be linked to the development of a short-lived extensional basin, fluvial drainage reorganization, and the establishment of the modern Yarlung River during early Miocene time (DeCelles et al., 2011; Wang et al., 2013; Carrapa et al., 2014; Lang and Huntington, 2014; Leary et al., 2016; Taylor et al., 2021; Ai et al., 2022).

If ZHe results in this study reflect exhumation in the Gangdese Range concurrent with Kailas Formation deposition, these data may provide additional constraints for future studies investigating the timing of Gangdese drainage divide formation. It is possible ZHe ages from this study are consistent with formation of the drainage divide at or near its

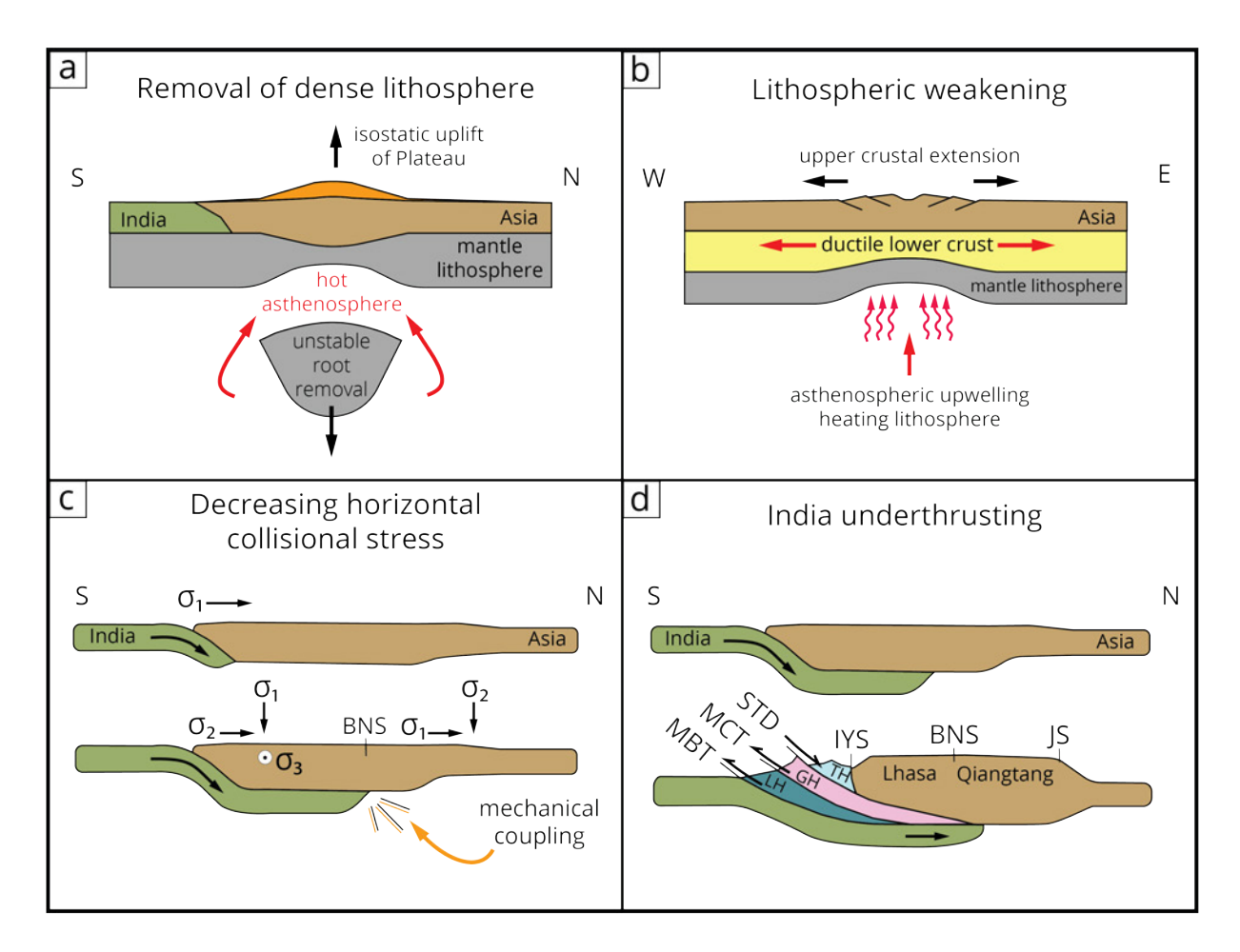


Figure 12 - Dynamic models for extension of the Tibetan Plateau: (a) Removal of an unstable dense lithospheric root causing isostatic uplift followed by gravitational collapse, triggering synchronous extension across the plateau; (b) Thermal weakening of the lithosphere due to asthenospheric upwelling and heating; (c) Decreasing horizontal collisional stress through mechanical coupling of Asian and Indian lithosphere causing the maximum principal stress σ 1 to rotate to vertical in southern Tibet; (d) Increasing crustal thickness by underthrusting Indian lithosphere beneath Asia to achieve a critical gravitational potential energy (GPE), leading to gravitational collapse of the plateau during Miocene time followed by a northward sweep in extension acceleration related to continued underthrusting of the Indian plate.

modern location along the crest of the Gangdese Range (Figure 2) and onset of internal drainage of the Tibetan plateau as early as ca. 28 Ma, but this is not required by the data. formation of Gangdese rifts during uplift of the Gangdese Range may have exerted some influence on drainage network patterns, but we posit the onset of rifting in the Gangdese Range is not a requirement or constraint for the timing of development of the Gangdese drainage divide. It has been suggested that Tibetan rifting and strike slip faulting in southern and central Tibet also contributes to fluvial reorganization through the diversion of river networks and relocation of lake centers, with a southward migration of the boundary between internal and external drainage of the Plateau hypothesized to have occurred since early Miocene time (Han et al., 2019; Taylor et al., 2021). It is possible that Gangdese rifting works to balance continued exhumation driven by contraction beneath the Gangdese Range (Sundell et al., 2021), which could in turn cause the location of the drainage divide to migrate from a more northward location during Oligocene to early-Miocene time to a more

southward location by late-Miocene time. In other words, the crest of the Gangdese Range may have shifted southwards through time due to continued surface uplift and exhumation balanced by Gangdese rifts. However, as the GT has not been documented in this region and the data in this study are merely consistent with this idea but do not require it, we suggest additional field observations and data collection in future studies are needed to test this hypothesis. Regardless, continued contraction beneath the Gangdese Range may be essential to explain the structural feasibility of continued uplift of Gangdese Range topography and existence of the modern day drainage divide in relation to ongoing contraction due to India-Asia collision (Laskowski et al., 2018; *Taylor et al.*, 2021). It is also possible that mantle delamination, lithospheric dripping, and other deep crustal or mantle processes act concurrently to the already complex interplay between surface uplift, exhumation, erosion, sedimentation, and climate to drive topographic change and enhanced basin subsidence in southern and central Tibet (Sobel and Strecker, 2003; Gao et al., 2013; Yin and Taylor, 2011; Bischoff and Flesch, 2018; Han et al.,

2019; Kapp and DeCelles, 2019; Taylor et al., 2021). We suggest future work including new geo- and thermochronology studies across southern Tibet and field observation of key structural interactions are essential for disentangling the complex tectonic interactions between extensional and contractional structures and their relation, if any, to the formation and evolution of drainage divides.

6 Conclusions

Tibet offers a unique opportunity to study synconvergent extension related to continental collision and to better understand the mechanics of early-stage continental rift initiation and development through time, offering a detailed account of the behavior and morphological expression of young or "failed" continental rifts. The TYC rift is bounded by two NNE striking (~N10°E-N35°E) high-angle (~45-70°) active normal faults that alternate dominance along strike. Footwall granodiorites show pervasive northeast dipping foliation, with slip lineations and fault plane striations indicating northeast directed oblique sinistral-normal slip. Analysis of 32 samples collected across key structural relationships in the southern TYC rift yielded 14 weighted mean U-Pb ages between \sim 59-49 Ma and 245 single-grain ZHe ages, with mean ZHe ages falling between \sim 60-4 Ma. Analysis of 17 samples collected from Gangdese rifts located \sim 90 km (GR1, five samples), \sim 75 km (GR2, ten samples), and \sim 40 km (GR3, two samples) east of TYC yielded ~85 single-grain ZHe ages with mean ages between ~28-16 Ma. Samples collected from Gangdese latitudes in southern TYC and Gangdese rifts show a concentration of Oligocene-early Miocene ages (\sim 28-16 Ma), whereas TYC rift samples north of ~29.8° latitude generated both younger late Miocene-Pliocene ages (~8-4 Ma) and older Paleocene-Eocene ages (∼60-48 Ma). We interpret the following: (1) Gangdese Range samples from TYC and Gangdese rifts likely reflect exhumation during contraction, uplift, and erosion along the GCT peaking at \sim 21-20 Ma, (2) \sim 8-4 Ma ages from TYC reflect extension timing along fault segments experiencing significant rift-related exhumation, and (3) \sim 60-48 Ma ages represent un-reset or partially reset samples from segments of the TYC rift that have experienced lesser magnitudes of rift exhumation. We interpret the U-Pb age of 16.1 \pm 0.1 Ma from an extensional dike to reflect a minimum age of onset for E-W extension in southern TYC, with continued and likely rapid rift exhumation through \sim 11 Ma reflected by crystallization of syn-extensional intrusive igneous bodies in southern TYC. HeFTy thermal models indicate a two-stage cooling history with initial slow cooling until \sim 16 Ma followed by accelerated cooling rates in late Miocene-Pliocene time (~13-4 Ma), consistent with results from previous studies of TYC and other Tibetan rifts. We interpret that the TYC rift evolved through fault segment linkage, followed by a northward sweeping acceleration of extension potentially related to underthrusting of the Indian plate beneath Tibet. This work contributes an unprecedented dataset for south-central Tibet including 18 U-Pb mean ages and ~245 single-grain ZHe ages from the southern TYC rift and neighboring Gangdese rifts and demonstrates the utility of low-temperature thermochronology methods to address major tectonic questions. Reported data and kinematic interpretations may be relevant to future studies investigating outstanding questions related to the early evolution of continental rifts. This study may also provide context for the investigation of extensional structures in other settings where synconvergent extension is documented, such as the North American Cordillera.

Acknowledgements

This work was funded by NSF Tectonics Awards to Dr. Andrew K. Laskowski (#1917685), Dr. Michael H. Taylor (#1917706), and Dr. Adam M. Forte (#1917695), and a GSA Graduate Student Research Grant award to PhD Candidate Aislin N. Reynolds. We thank Dr. Peter Reiners and Dr. Uttam Chowdhury at the ARHDL for ZHe sample analyses and staff of the Arizona LaserChron Center for U-Pb sample analyses and data interpretation.

Author contributions

Aislin N. Reynolds: conception of study, investigation, methodology, funding acquisition, writing-original draft. Andrew K. Laskowski: conception of study, investigation, supervision, funding acquisition, writing-review and editing. Caden J. Howlett: investigation, writing-review and editing. Devon A. Orme: methodology, Kurt E. Sundell: investigation, writing-review. writing-review. Michael H. Taylor: conception of study, funding acquisition, writing-review. Adam M. Forte: conception of study, funding acquisition, writing-review. Spencer Dixon: creation of map in Figure 2, writing-review. Fulong Cai: permitting, **Guo Xudong:** investigation. investigation, methodology. **Ding Lin**: permitting, methodology.

Data availability

Supplementary data are included in the Supporting Information published with this manuscript. Data tables from this research are available online through an open source repository (DOI: 10.5281/zenodo.10003842). Provided spreadsheets include location and lithology information and mean ages for all samples (Table 1), igneous U-Pb data tables for all analyzed samples (Table S2), and zircon (U-Th)/He data tables for all analyzed samples (Table S3). Supplementary figures include a compilation of previous studies with published geo- and thermochronology data in the Tangra Yumco Rift region (Figure S1, data source DOI:

10.1002/2017GC007217), weighted mean plots for all igneous zircon U-Pb analyses (Figure S2), plots of zircon (U-Th)/He data showing age as a function of grain size and age as a function of effective uranium (Figure S3), and HeFTy models (resulting thermal history paths and envelopes) for all samples (Figure S4). Geologic map was drafted over hill shade and slope maps generated in ArcGIS Pro, derived from Shuttle Radar Topography Mission (SRTM) 1 Arc-Second Global Digital Elevation data (DOI:/10.5066/F7PR7TFT) and draped Landsat Legacy Global Land Survey (GLS) imagery (DOI: 10.5066/F7M32TQB).

Competing interests

The authors declare no competing interests.

Peer review

This publication was peer-reviewed by Anne Replumaz, Konstanze Stübner, and Reinhard Wolff. The full peer-review report can be found here: tektonika.online/index.php/home/article/view/42/92

Copyright notice

© Author(s) 2024. This article is distributed under the Creative Commons Attribution 4.0 International License, which permits unrestricted use, distribution, and reproduction in any medium, provided the original author(s) and source are credited, and any changes made are indicated.

References

- Ai, K., K. Zhang, B. Song, T. Shen, and J. Ji (2022), Upper Oligocene–Lower miocene gangdese conglomerate along the Yarlung-Zangbo suture zone and its implications for Palaeo-Yarlung-Zangbo initiation, *Frontiers of Earth Science in China*, *10*, doi: 10.3389/feart.2022.808843.
- Aitchison, J., A. M. Davis, Badengzhu, and H. Luo (2002), New constraints on the India–Asia collision: the lower miocene gangrinboche conglomerates, yarlung tsangpo suture zone, SE tibet, *Journal of Asian Earth Sciences*, *21*(3), 251–263, doi: 10.1016/S1367-9120(02)00037-8.
- Allmendinger, R. W. (1986), Tectonic development, southeastern border of the puna plateau, northwestern argentine andes, *Geological Society of America bulletin*, *97*(9), 1070, doi: 10.1130/0016-7606(1986)97<1070:tdsbot>2.0.co;2.
- An, W., X. Hu, E. Garzanti, M. K. BouDagher-Fadel, J. Wang, and G. Sun (2014), Xigaze forearc basin revisited (south tibet): Provenance changes and origin of the xigaze ophiolite, *Geological Society of America bulletin*, 126(11-12), 1595–1613, doi: 10.1130/b31020.1.
- Anders, M. H., and R. W. Schlische (1994), Overlapping faults, intrabasin highs, and the growth of normal faults, *The Journal of geology*, *102*(2), 165–179, doi: 10.1086/629661.

- Armijo, R., P. Tapponnier, J. L. Mercier, and T.-L. Han (1986), Quaternary extension in southern tibet: Field observations and tectonic implications, *Journal of geophysical research*, *91*(B14), 13,803–13,872, doi: 10.1029/jb091ib14p13803.
- Ault, A., C. Gautheron, and G. King (2019), Innovations in (U–Th)/He, fission track, and trapped charge thermochronometry with applications to earthquakes, weathering, surface-mantle connections, and the growth and decay of mountains, *Tectonics*, *38*(11), 3705–3739, doi: 10.1029/2018TC005312.
- Axen, G., J. Fletcher, E. Cowgill, M. Murphy, P. Kapp, I. Macmillan, E. Ramos-Velázquez, and J. Aranda-Gómez (1999), Range-front fault scarps of the sierra el mayor, baja california: Formed above an active low-angle normal fault?, *Geology*, *27*(3), 247–250, doi: 10.1130/0091-7613(1999)027<0247:RFFSOT>2.3.CO;2.
- Bian, S., J. Gong, A. Zuza, R. Yang, L. Chen, J. Ji, X. Yu, Y. Tian, Z. Yu, X. Cheng, X. Lin, and H. Chen (2022), Along-strike variation in the initiation timing of the north-trending rifts in southern tibet as revealed from the Yadong-Gulu rift, *Tectonics*, *41*(7), e2021TC007,091, doi: 10.1029/2021TC007091.
- Bischoff, S. H., and L. M. Flesch (2018), Normal faulting and viscous buckling in the tibetan plateau induced by a weak lower crust, *Nature communications*, *9*(1), 4952, doi: 10.1038/s41467-018-07312-9.
- Black, L. P., S. L. Kamo, C. M. Allen, D. W. Davis, J. N. Aleinikoff, J. W. Valley, R. Mundil, I. H. Campbell, R. J. Korsch, I. S. Williams, and Others (2004), Improved 206Pb/238U microprobe geochronology by the monitoring of a trace-element-related matrix effect; SHRIMP, ID-TIMS, ELA-ICP-MS and oxygen isotope documentation for a series of zircon standards, *Chemical geology*, 205(1-2), 115–140.
- Blisniuk, P. M., B. R. Hacker, J. Glodny, L. Ratschbacher, S. Bi, Z. Wu, M. O. McWilliams, and A. Calvert (2001), Normal faulting in central tibet since at least 13.5 myr ago, *Nature*, *412*(6847), 628–632, doi: 10.1038/35088045.
- Braun, J. (2003), Pecube: a new finite-element code to solve the 3D heat transport equation including the effects of a time-varying, finite amplitude surface topography, *Computers & geosciences*, *29*(6), 787–794, doi: 10.1016/s0098-3004(03)00052-9.
- Braun, J., P. van der Beek, P. Valla, X. Robert, F. Herman, C. Glotzbach, V. Pedersen, C. Perry, T. Simon-Labric, and C. Prigent (2012), Quantifying rates of landscape evolution and tectonic processes by thermochronology and numerical modeling of crustal heat transport using PECUBE, *Tectonophysics*, *524-525*, 1–28, doi: 10.1016/j.tecto.2011.12.035.
- Brune, S., F. Kolawole, J. Olive, D. S. Stamps, W. Buck, S. Buiter, T. Furman, and D. Shillington (2023), Geodynamics of continental rift initiation and evolution, *Nature reviews. Earth & environment, 4*(4), 235–253, doi: 10.1038/s43017-023-00391-3.
- Buck, W. R. (1988), Flexural rotation of normal faults, *Tectonics*, 7(5), 959–973, doi: 10.1029/tc007i005p00959.
- Buck, W. R. (1991), Modes of continental lithospheric extension, *Journal of geophysical research*, *96*(B12), 20,161–20,178, doi: 10.1029/91jb01485.
- Buck, W. R. (1993), Effect of lithospheric thickness on the formation of high- and low-angle normal faults, *Geology*, *21*(10), 933–936, doi:

10.1130/0091-7613(1993)021<0933:EOLTOT>2.3.CO;2.

- Burchfiel, В. C., and L. H. Royden (1985), North-south extension within the convergent himalayan region, Geology, *13*(10), 679, doi: 10.1130/0091-7613(1985)13<679:newtch>2.0.co;2.
- Burchfiel, B. C., C. Zhiliang, K. V. Hodges, L. Yuping, L. H. Royden, D. Changrong, and X. Jiene (1992), The South Tibetan Detachment System, Himalayan Orogen: Extension Contemporaneous With and Parallel to Shortening in a Collisional Mountain Belt, in *The South Tibetan Detachment System, Himalayan Orogen: Extension Contemporaneous With and Parallel to Shortening in a Collisional Mountain Belt*, Geological Society of America, doi: 10.1130/SPE269-p1.
- Burg, J., F. Proust, P. Tapponnier, and C. Ming (1983), Deformation phases and tectonic evolution of the lhasa block (southern tibet, china), *Eclogae Geologicae Helvetiae*, 76(3), 643–665.
- Burke, W. B., A. Laskowski, D. Orme, K. Sundell, M. Taylor, X. Guo, and L. Ding (2021), Record of crustal thickening and synconvergent extension from the dajiamang tso rift, southern tibet, *Géosciences*, *11*(5), 209, doi: 10.3390/GEOSCIENCES11050209.
- Carrapa, B., D. A. Orme, P. G. DeCelles, P. Kapp, M. A. Cosca, and R. Waldrip (2014), Miocene burial and exhumation of the India-Asia collision zone in southern tibet: Response to slab dynamics and erosion, *Geology*, *42*(5), 443–446, doi: 10.1130/g35350.1.
- Chevalier, M., P. Tapponnier, J. Woerd, P. Leloup, S. Wang, J. Pan, M. Bai, E. Kali, X. Liu, and H. Li (2019), Late quaternary extension rates across the northern half of the Yadong-Gulu rift: Implication for east-west extension in southern tibet, *Journal of Geophysical Research*, *[Solid Earth]*, *125*(7), e2019JB019,106, doi: 10.1029/2019JB019106.
- Cogan, M. J., K. D. Nelson, W. S. F. Kidd, and C. Wu (1998), Shallow structure of the Yadong-Gulu rift, southern tibet, from refraction analysis of project INDEPTH common midpoint data, *Tectonics*, *17*(1), 46–61, doi: 10.1029/97tc03025.
- Coleman, M., and K. Hodges (1995), Evidence for tibetan plateau uplift before 14 myr ago from a new minimum age for east–west extension, *Nature*, *374*(6517), 49–52, doi: 10.1038/374049A0.
- Copley, A., J.-P. Avouac, and B. P. Wernicke (2011), Evidence for mechanical coupling and strong indian lower crust beneath southern tibet, *Nature*, *472*(7341), 79–81, doi: 10.1038/nature09926.
- Corfu, F., J. Hanchar, P. Hoskin, and P. Kinny (2003), Atlas of zircon textures, *Reviews in Mineralogy and Geochemistry*, 53(1), 469–500, doi: 10.2113/0530469.
- Curry, M. A. E., J. B. Barnes, and J. P. Colgan (2016), Testing fault growth models with low-temperature thermochronology in the northwest basin and range, USA, *Tectonics*, *35*(10), 2467–2492, doi: 10.1002/2016tc004211.
- DeCelles, P., P. Kapp, J. Quade, and G. Gehrels (2011), Oligocene-Miocene kailas basin, southwestern tibet: Record of postcollisional upper-plate extension in the Indus-Yarlung suture zone, *Geological Society of America bulletin*, 123(7-8), 1337–1362, doi: 10.1130/B30258.1.
- DeCelles, P. G., D. M. Robinson, and G. Zandt (2002), Implications of shortening in the himalayan fold-thrust belt for uplift of the tibetan plateau, *Tectonics*, *21*(6),

- 12-1-12-25, doi: 10.1029/2001tc001322.
- DeCelles, P. G., B. Carrapa, G. E. Gehrels, T. Chakraborty, and P. Ghosh (2016), Along-strike continuity of structure, stratigraphy, and kinematic history in the himalayan thrust belt: The view from northeastern india, *Tectonics*, *35*(12), 2995–3027, doi: 10.1002/2016tc004298.
- Dodson, M. H. (1973), Closure temperature in cooling geochronological and petrological systems, *Contributions to mineralogy and petrology. Beitrage zur Mineralogie und Petrologie*, 40(3), 259–274, doi: 10.1007/bf00373790.
- Dürr, S. B. (1996), Provenance of xigaze fore-arc basin clastic rocks (cretaceous, south tibet), *Geological Society of America bulletin*, *108*(6), 669–684, doi: 10.1130/0016-7606(1996)108<0669:poxfab>2.3.co;2.
- Einsele, G., B. Liu, S. Durr, W. Frisch, G. Liu, H. Luterbacher, L. Ratschbacher, W. Ricken, J. Wendt, A. Wetzel, G. Yu, and H. Zheng (1994), The xigaze forearc basin: evolution and facies architecture (cretaceous, tibet), *Sedimentary geology*, *90*(1-2), 1–32, doi: 10.1016/0037-0738(94)90014-0.
- England, P., and G. Houseman (1989), Extension during continental convergence, with application to the tibetan plateau, *Journal of geophysical research*, *94*(B12), 17,561–17,579, doi: 10.1029/jb094ib12p17561.
- England, and P. Molnar (1990), Surface uplift, uplift of rocks, and exhumation of rocks, Geology, 18(12), 1173, doi: 10.1130/0091-7613(1990)018<1173:suuora>2.3.co;2.
- England, P., and M. Searle (1986), The cretaceous-tertiary deformation of the lhasa block and its implications for crustal thickening in tibet, *Tectonics*, *5*(1), 1–14, doi: 10.1029/tc005i001p00001.
- Farley, K. A., R. A. Wolf, and L. T. Silver (1996), The effects of long alpha-stopping distances on (U-Th)/He ages, *Geochimica et cosmochimica acta*, 60(21), 4223–4229, doi: 10.1016/s0016-7037(96)00193-7.
- Faulds, J. E., R. J. Varga, and J. H. Stewart (1998), The role of accommodation zones and transfer zones in the regional segmentation of extended terranes, *Special papers-Geological*, pp. 1–46.
- Fielding, E., B. Isacks, M. Barazangi, and C. Duncan (1994), How flat is tibet?, *Geology*, *22*(2), 163, doi: 10.1130/0091-7613(1994)022<0163:hfit>2.3.co;2.
- Gan, W., P. Zhang, Z.-K. Shen, Z. Niu, M. Wang, Y. Wan, D. Zhou, and J. Cheng (2007), Present-day crustal motion within the tibetan plateau inferred from GPS measurements, *Journal of geophysical research*, *112*(B8), doi: 10.1029/2005jb004120.
- Gansser, A. (1964), *Geology of the Himalayas*, Interscience Publishers, a division of John Wiley, London, New York, Sydney (tr. Zurich).
- Gao, R., C. Chen, Z. Lu, L. D. Brown, X. Xiong, W. Li, and G. Deng (2013), New constraints on crustal structure and moho topography in central tibet revealed by SinoProbe deep seismic reflection profiling, *Tectonophysics*, 606, 160–170, doi: 10.1016/j.tecto.2013.08.006.
- Gao, T., Z. Ding, X. Wang, and L. Jiang (2021), Joint inversion of receiver functions, rayleigh wave dispersion and ZH ratio for crustal structure in southeast tibetan plateau and its implications for dynamics, *Chinese journal of geophysics*, *64*(6), 1885–1906.
- Garzione, C. N., P. G. DeCelles, D. G. Hodkinson, T. P. Ojha, and B. N. Upreti (2003), East-west extension

- and miocene environmental change in the southern tibetan plateau: Thakkhola graben, central nepal, *Geological Society of America bulletin*, *115*(1), 3–20, doi: 10.1130/0016-7606(2003)115<0003:eweame>2.0.co;2.
- Gehrels, G., V. Valencia, and A. Pullen (2006), Detrital zircon geochronology by laser-ablation multicollector ICPMS at the arizona LaserChron center, *The Paleontological Society Papers*, 12, 67–76.
- Gehrels, G., V. Valencia, and J. Ruíz (2008), Enhanced precision, accuracy, efficiency, and spatial resolution of U-Pb ages by laser ablation–multicollector–inductively coupled plasma–mass spectrometry, *Geochemistry: Exploration, Environment, Analysis*, *9*(3), doi: 10.1029/2007GC001805.
- Gehrels, G., M. Rusmore, G. Woodsworth, M. Crawford, C. Andronicos, L. Hollister, J. Patchett, M. Ducea, R. Butler, K. Klepeis, and Others (2009), U-Th-Pb geochronology of the coast mountains batholith in north-coastal british columbia: Constraints on age and tectonic evolution, *Geological Society of America bulletin*, 121(9-10), 1341–1361.
- Gehrels, G. E. (2009), Age pick program.
- Geng, Q.-R., Z.-M. Sun, G.-T. Pan, D.-C. Zhu, and L.-Q. Wang (2009), Origin of the gangdise (transhimalaya) permian arc in southern tibet: Stratigraphic and volcanic geochemical constraints, *Island Arc*, *18*(3), 467–487, doi: 10.1111/j.1440-1738.2009.00664.x.
- Giovanni, M. K., B. K. Horton, C. N. Garzione, B. McNulty, and M. Grove (2010), Extensional basin evolution in the cordillera blanca, peru: Stratigraphic and isotopic records of detachment faulting and orogenic collapse in the andean hinterland, *Tectonics*, *29*(6), doi: 10.1029/2010tc002666.
- Guenthner, W. R., P. W. Reiners, R. A. Ketcham, L. Nasdala, and G. Giester (2013), Helium diffusion in natural zircon: Radiation damage, anisotropy, and the interpretation of zircon (U-Th)/He thermochronology, *American journal of science*, 313(3), 145–198, doi: 10.2475/03.2013.01.
- Ha, G., Z. Wu, and F. Liu (2019), Late quaternary vertical slip rates along the southern Yadong–Gulu rift, southern tibetan plateau, *Tectonophysics*, *755*, 75–90, doi: 10.1016/J.TECTO.2019.02.014.
- Hager, C., D. F. Stockli, T. J. Dewane, G. Gehrels, and L. Ding (2009), Anatomy and crustal evolution of the central lhasa terrane (S-Tibet) revealed by investigations in the xainza rift, in *EGU General Assembly Conference Abstracts*, p. 11346.
- Han, Z., H. D. Sinclair, Y. Li, C. Wang, Z. Tao, X. Qian, Z. Ning, J. Zhang, Y. Wen, J. Lin, and Others (2019), Internal drainage has sustained low-relief tibetan landscapes since the early miocene, *Geophysical research letters*, 46(15), 8741–8752.
- Harley, S. L., N. M. Kelly, and A. Moller (2007), Zircon behaviour and the thermal histories of mountain chains, *Elements*, *3*(1), 25–30, doi: 10.2113/gselements.3.1.25.
- Harrison, T. M., P. Copeland, W. S. F. Kidd, and O. M. Lovera (1995), Activation of the nyainqentanghla shear zone: Implications for uplift of the southern tibetan plateau, *Tectonics*, *14*(3), 658–676, doi: 10.1029/95tc00608.
- Harrison, T. M., A. Yin, M. Grove, O. M. Lovera, F. J. Ryerson, and X. Zhou (2000), The zedong window: A record of superposed tertiary convergence in southeastern tibet, *Journal of geophysical research*, *105*(B8), 19,211–19,230, doi: 10.1029/2000jb900078.

- He, S., P. Kapp, P. DeCelles, G. Gehrels, and M. Heizler (2007), Cretaceous-Tertiary geology of the gangdese arc in the linzhou area, southern tibet, *Tectonophysics*, 433(1-4), 15–37, doi: 10.1016/J.TECTO.2007.01.005.
- Heim, A., and A. Gansser (1975), *Central Himalaya: Geological observations of the Swiss expedition, 1936*, vol. 73, Hindustan Publishing Corporation (India).
- Hoskin, P. W. O., and U. Schaltegger (2003), The composition of zircon and igneous and metamorphic petrogenesis, *Reviews in Mineralogy and Geochemistry*, 53(1), 27–62.
- Hou, Z., Y. Gao, X. Qu, Z. Rui, and X. Mo (2004), Origin of adakitic intrusives generated during mid-miocene east–west extension in southern tibet, *Earth and planetary science letters*, *220*(1-2), 139–155, doi: 10.1016/S0012-821X(04)00007-X.
- Hourigan, J. K., P. W. Reiners, and M. T. Brandon (2005), U-Th zonation-dependent alpha-ejection in (U-Th)/He chronometry, *Geochimica et cosmochimica acta*, *69*(13), 3349–3365, doi: 10.1016/j.gca.2005.01.024.
- Huang, F., M. Li, J. Xu, Y. Zeng, J. Chen, B. Wang, H. Yu, L.-K. Chen, P. Zhao, and Z. Zhang (2019), Geodynamic transition from subduction to extension: evidence from the geochronology and geochemistry of granitoids in the sangsang area, southern lhasa terrane, tibet, *International Journal of Earth Sciences*, *108*, 1663–1681, doi: 10.1007/s00531-019-01729-3.
- Huang, W., G. Dupont-Nivet, P. Lippert, D. Hinsbergen, and E. Hallot (2013), Inclination shallowing in eocene linzizong sedimentary rocks from southern tibet: correction, possible causes and implications for reconstructing the India–Asia collision, *Geophysical Journal International*, 194(3), 1390–1411, doi: 10.1093/GJI/GGT188.
- Hughes, C. A., M. J. Jessup, C. A. Shaw, and D. L. Newell (2019), Deformation conditions during syn-convergent extension along the cordillera blanca shear zone, peru, *Geosphere*, *15*(4), 1342–1367, doi: 10.1130/ges02040.1.
- Huntington, K., and K. Klepeis (2018), Challenges and opportunities for research in tectonics: Understanding deformation and the processes that link earth systems, from geologic time to human time. a community vision document submitted to the U.S. national science foundation, *Tech. rep.*, University of Washington.
- Husson, L., M. Bernet, S. Guillot, P. Huyghe, J.-L. Mugnier, A. Replumaz, X. Robert, and P. Van der Beek (2014), Dynamic ups and downs of the himalaya, *Geology*, *42*(10), 839–842, doi: 10.1130/G36049.1.
- Jessup, M. J., D. L. Newell, J. M. Cottle, A. L. Berger, and J. A. Spotila (2008), Orogen-parallel extension and exhumation enhanced by denudation in the trans-himalayan arun river gorge, ama drime massif, Tibet-Nepal, *Geology*, *36*(7), 587, doi: 10.1130/g24722a.1.
- Ji, W., F.-Y. Wu, S. Chung, J. Li, and C.-Z. Liu (2009), Zircon U-Pb geochronology and hf isotopic constraints on petrogenesis of the gangdese batholith, southern tibet, *Chemical geology*, *262*(3-4), 229–245, doi: 10.1016/J.CHEMGEO.2009.01.020.
- Kali, E., P. H. Leloup, N. Arnaud, G. Mahéo, D. Liu, E. Boutonnet, J. Van der Woerd, X. Liu, J. Liu-Zeng, and H. Li (2010), Exhumation history of the deepest central himalayan rocks, ama drime range: Key pressure-temperature-deformation-time constraints on orogenic models, *Tectonics*, *29*(2).
- Kapp, J. L. D., T. M. Harrison, P. Kapp, M. Grove, O. M. Lovera,

- and D. Lin (2005), Nyainqentanglha shan: A window into the tectonic, thermal, and geochemical evolution of the lhasa block, southern tibet, *Journal of geophysical research*, *110*(B8), doi: 10.1029/2004jb003330.
- Kapp, P., and P. G. DeCelles (2019), Mesozoic–Cenozoic geological evolution of the Himalayan-Tibetan orogen and working tectonic hypotheses, *American journal of science*, *319*(3), 159–254.
- Kapp, P., and J. H. Guynn (2004), Indian punch rifts tibet, *Geology*, *32*(11), 993, doi: 10.1130/g20689.1.
- Kapp, P., P. DeCelles, A. Leier, J. Fabijanic, S. He, A. Pullen, G. Gehrels, and L. Ding (2007), The gangdese retroarc thrust belt revealed, *GSA today: a publication of the Geological Society of America*, *17*(7), 4–9, doi: 10.1130/GSAT01707A.1.
- Kapp, P., M. Taylor, D. Stockli, and L. Ding (2008), Development of active low-angle normal fault systems during orogenic collapse: Insight from tibet, *Geology*, *36*(4), 336, doi: 10.1130/0091-7613(2008)36[336:doalnf]2.0.co;2.
- Kay, R. W., and S. Mahlburg Kay (1993), Delamination and delamination magmatism, *Tectonophysics*, *219*(1-3), 177–189, doi: 10.1016/0040-1951(93)90295-u.
- Ketcham, R., C. Gautheron, and L. Tassan-got (2011), Accounting for long alpha-particle stopping distances in (U–Th–Sm)/He geochronology: Refinement of the baseline case, *Geochimica et cosmochimica acta*, *75*(24), 7779–7791, doi: 10.1016/J.GCA.2011.10.011.
- Ketcham, R. A. (2005), Forward and inverse modeling of low-temperature thermochronometry data, *Reviews in Mineralogy and Geochemistry*, *58*(1), 275–314, doi: 10.2138/rmg.2005.58.11.
- Kind, R., X. Yuan, J. Saul, D. Nelson, S. V. Sobolev, J. Mechie, W. Zhao, G. Kosarev, J. Ni, U. Achauer, and M. Jiang (2002), Seismic images of crust and upper mantle beneath tibet: evidence for eurasian plate subduction, *Science*, 298(5596), 1219–1221, doi: 10.1126/science.1078115.
- Klemperer, S., P. Zhao, C. Whyte, T. Darrah, L. Crossey, K. Karlstrom, T. Liu, C. Winn, D. Hilton, and L. Ding (2022), Limited underthrusting of india below tibet: 3He/4He analysis of thermal springs locates the mantle suture in continental collision, *Proceedings of the National Academy of Sciences of the United States of America*, 119(12), e2113877,119, doi: 10.1073/pnas.2113877119.
- Labrousse, L., B. Huet, L. Le Pourhiet, L. Jolivet, and E. Burov (2016), Rheological implications of extensional detachments: Mediterranean and numerical insights, *Earth-science reviews*, *161*, 233–258, doi: 10.1016/j.earscirev.2016.09.003.
- Lang, K., and K. Huntington (2014), Antecedence of the yarlung–siang–brahmaputra river, eastern himalaya, *Earth and planetary science letters*, *397*, 145–158, doi: 10.1016/J.EPSL.2014.04.026.
- Laskowski, A., P. Kapp, L. Ding, C. Campbell, and X. Liu (2017), Tectonic evolution of the yarlung suture zone, lopu range region, southern tibet, *Tectonics*, *36*(1), 108–136, doi: 10.1002/2016TC004334.
- Laskowski, A. K., P. Kapp, and F. Cai (2018), Gangdese culmination model: Oligocene–Miocene duplexing along the India-Asia suture zone, lazi region, southern tibet, *GSA Bulletin*, *130*(7-8), 1355–1376.
- Leary, R., D. A. Orme, A. K. Laskowski, P. G. DeCelles, P. Kapp, B. Carrapa, and M. Dettinger (2016), Along-strike diachroneity in deposition of the kailas formation

- in central southern tibet: Implications for indian slab dynamics, *Geosphere*, *12*(4), 1198–1223, doi: 10.1130/ges01325.1.
- Lee, H. Y., S. L. Chung, C. H. Lo, J. Ji, D. J. Wen, Q. Qian, T. Y. Lee, and Q. Zhang (2007), On the age and geodynamic significance of the linzizong volcanic successions, southern tibet: Neo-Tethyan slab breakoff in the early stage of the India-Asia collision.
- Lee, H.-Y., S.-L. Chung, C.-H. Lo, J. Ji, T.-Y. Lee, Q. Qian, and Q. Zhang (2009), Eocene neotethyan slab breakoff in southern tibet inferred from the linzizong volcanic record, *Tectonophysics*, *477*(1-2), 20–35, doi: 10.1016/j.tecto.2009.02.031.
- Lee, H.-Y., S. Chung, J. Ji, Q. Qian, S. Gallet, C. Lo, T. Lee, and Q. Zhang (2012), Geochemical and Sr–Nd isotopic constraints on the genesis of the cenozoic linzizong volcanic successions, southern tibet, *Journal of Asian Earth Sciences*, *53*, 96–114, doi: 10.1016/J.JSEAES.2011.08.019.
- Lee, J., C. Hager, S. R. Wallis, D. F. Stockli, M. J. Whitehouse, M. Aoya, and Y. Wang (2011), Middle to late miocene extremely rapid exhumation and thermal reequilibration in the kung co rift, southern tibet, *Tectonics*, *30*(2), doi: 10.1029/2010tc002745.
- Leier, A. L., P. G. DeCelles, P. Kapp, and G. E. Gehrels (2007), Lower cretaceous strata in the lhasa terrane, tibet, with implications for understanding the early tectonic history of the tibetan plateau, *Journal of Sedimentary Research*, 77(10), 809–825, doi: 10.2110/jsr.2007.078.
- Li, G., B. Kohn, M. Sandiford, Z. Xu, and L. Wei (2015), Constraining the age of liuqu conglomerate, southern tibet: Implications for evolution of the India-Asia collision zone, *Earth and planetary science letters*, *426*, 259–266, doi: 10.1016/J.EPSL.2015.06.010.
- Li, S., C. Guilmette, L. Ding, Q. Xu, J.-J. Fu, and Y.-H. Yue (2017), Provenance of mesozoic clastic rocks within the Bangong-Nujiang suture zone, central tibet: Implications for the age of the initial Lhasa-Qiangtang collision, *Journal of Asian Earth Sciences*, *147*, 469–484, doi: 10.1016/j.jseaes.2017.08.019.
- Li, Y., C. Wang, H. Yi, B. Deng, C. Liu, X. Yang, S. Lai, and W. Fang (2001), Characteristics of the shuanghu graben and cenozoic extension in northern tibet, *Science in China. Series D, Earth sciences / Chinese Academy of Sciences*, *44*(S1), 284–291, doi: 10.1007/bf02911998.
- Liu, A.-L., Q. Wang, D.-C. Zhu, Z.-D. Zhao, S.-A. Liu, R. Wang, J.-G. Dai, Y.-C. Zheng, and L.-L. Zhang (2018), Origin of the ca. 50 ma linzizong shoshonitic volcanic rocks in the eastern gangdese arc, southern tibet, *Lithos*, *304-307*, 374–387, doi: 10.1016/j.lithos.2018.02.017.
- Long, S. P., S. N. Thomson, P. W. Reiners, and R. V. Di Fiori (2015), Synorogenic extension localized by upper-crustal thickening: An example from the late cretaceous nevadaplano, *Geology*, *43*(4), 351–354, doi: 10.1130/g36431.1.
- Maheo, G., P. Leloup, F. Valli, R. Lacassin, N. Arnaud, J. Paquette, A. Fernandez, L. Haibing, K. Farley, and P. Tapponnier (2007), Post 4 ma initiation of normal faulting in southern tibet. constraints from the kung co half graben, *Earth and planetary science letters*, *256*(1-2), 233–243, doi: 10.1016/j.epsl.2007.01.029.
- Marrett, R., and M. R. Strecker (2000), Response of intracontinental deformation in the central andes to late cenozoic reorganization of south american

- plate motions, *Tectonics*, *19*(3), 452–467, doi: 10.1029/1999tc001102.
- McCaffrey, R., and J. Nabelek (1998), Role of oblique convergence in the active deformation of the himalayas and southern tibet plateau, *Geology*, *26*(8), 691, doi: 10.1130/0091-7613(1998)026<0691:roocit>2.3.co;2.
- McCallister, A. T., M. H. Taylor, M. A. Murphy, R. H. Styron, and D. F. Stockli (2014), Thermochronologic constraints on the late cenozoic exhumation history of the gurla mandhata metamorphic core complex, southwestern tibet, *Tectonics*, 33(2), 27–52, doi: 10.1002/2013tc003302.
- Mo, X., Y. Niu, G. Dong, Z. Zhao, Z. Hou, S. Zhou, and S. Ke (2008), Contribution of syncollisional felsic magmatism to continental crust growth: A case study of the paleogene linzizong volcanic succession in southern tibet, *Chemical geology*, 250(1-4), 49–67, doi: 10.1016/j.chemgeo.2008.02.003.
- Molnar, P., and P. Tapponnier (1978), Active tectonics of tibet, *Journal of geophysical research*, *83*(B11), 5361–5375, doi: 10.1029/jb083ib11p05361.
- Molnar, P., P. England, and J. Martinod (1993), Mantle dynamics, uplift of the tibetan plateau, and the indian monsoon, *Reviews of geophysics*, *31*(4), 357–396, doi: 10.1029/93rg02030.
- Murphy, M., V. I. Sanchez, and M. Taylor (2010), Syncollisional extension along the India-Asia suture zone, south-central tibet: Implications for crustal deformation of tibet, *Earth and planetary science letters*, 290(3-4), 233–243, doi: 10.1016/J.EPSL.2009.11.046.
- Murphy, M. A., A. Yin, P. Kapp, T. M. Harrison, C. E. Manning, F. J. Ryerson, D. Lin, and G. Jinghui (2002), Structural evolution of the gurla mandhata detachment system, southwest tibet: Implications for the eastward extent of the karakoram fault system, *Geological Society of America bulletin*, 114(4), 428–447, doi: 10.1130/0016-7606(2002)114<0428:seotgm>2.0.co;2.
- Nábelek, J., G. Hetényi, J. Vergne, S. Sapkota, B. Kafle, M. Jiang, H. Su, J. Chen, B.-S. Huang, and Hi-CLIMB Team (2009), Underplating in the Himalaya-Tibet collision zone revealed by the Hi-CLIMB experiment, *Science*, *325*(5946), 1371–1374, doi: 10.1126/science.1167719.
- Orme, D., and A. Laskowski (2016), Basin analysis of the Albian–Santonian xigaze forearc, lazi region, South-Central tibet, *Journal of Sedimentary Research*, 86(8), 894–913, doi: 10.2110/JSR.2016.59.
- Orme, D. A. (2019), Burial and exhumation history of the xigaze forearc basin, yarlung suture zone, tibet, *Geoscience frontiers*, *10*(3), 895–908, doi: 10.1016/j.gsf.2017.11.011.
- Orme, D. A., B. Carrapa, and P. Kapp (2015), Sedimentology, provenance and geochronology of the upper cretaceous–lower eocene western xigaze forearc basin, southern tibet, *Basin Research*, *27*(4), 387–411.
- Owens, T. J., and G. Zandt (1997), Implications of crustal property variations for models of tibetan plateau evolution, *Nature*, *387*(6628), 37–43, doi: 10.1038/387037a0.
- Paces, J. B., and J. D. Miller, Jr (1993), Precise U-Pb ages of duluth complex and related mafic intrusions, northeastern minnesota: Geochronological insights to physical, petrogenetic, paleomagnetic, and tectonomagmatic processes associated with the 1.1 ga midcontinent rift system, *Journal of geophysical research*, 98(B8), 13,997–14,013, doi: 10.1029/93jb01159.

- Pan, G. T., J. Ding, D. S. Yao, and . W. L. Q. (2004), Geological map of the tibetan plateau and adjacent areas (1:1,500,000).
- Pan, Y., and W. S. F. Kidd (1992), Nyainqentanglha shear zone: A late miocene extensional detachment in the southern tibetan plateau, *Geology*, *20*(9), 775, doi: 10.1130/0091-7613(1992)020<0775:nszalm>2.3.co;2.
- Patriat, P., and J. Achache (1984), India–Eurasia collision chronology has implications for crustal shortening and driving mechanism of plates, *Nature*, *311*(5987), 615–621, doi: 10.1038/311615A0.
- Platt, J. P., and P. C. England (1994), Convective removal of lithosphere beneath mountain belts; thermal and mechanical consequences, *American journal of science*, 294(3), 307–336, doi: 10.2475/ajs.294.3.307.
- Pullen, A., M. Ibáñez-Mejia, G. E. Gehrels, D. Giesler, and M. Pecha (2018), Optimization of a laser ablation-single collector-inductively coupled plasma-mass spectrometer (thermo element 2) for accurate, precise, and efficient zircon U-Th-Pb geochronology, *Geochemistry, Geophysics, Geosystems*, 19(10), 3689–3705, doi: 10.1029/2018gc007889.
- Ratschbacher, L., W. Frisch, C. Chen, and G. Pan (1992), Deformation and motion along the southern margin of the lhasa block (tibet) prior to and during the India-Asia collision, *Journal of Geodynamics*, *16*(1-2), 21–54, doi: 10.1016/0264-3707(92)90017-m.
- Ratschbacher, L., W. Frisch, G. Liu, and C. Chen (1994), Distributed deformation in southern and western tibet during and after the India-Asia collision, *Journal of geophysical research*, *99*(B10), 19,917–19,945, doi: 10.1029/94jb00932.
- Ratschbacher, L., I. Krumrei, M. Blumenwitz, M. Staiger, R. Gloaguen, B. V. Miller, S. D. Samson, M. A. Edwards, and E. Appel (2011), Rifting and strike-slip shear in central tibet and the geometry, age and kinematics of upper crustal extension in tibet, *Geological Society, London, Special Publications*, 353(1), 127–163.
- Reiners, P., and K. Farley (2001), Influence of crystal size on apatite (U-Th)/He thermochronology: an example from the bighorn mountains, wyoming, *Earth and planetary science letters*, *188*(3-4), 413–420, doi: 10.1016/S0012-821X(01)00341-7.
- Reiners, P., K. Farley, and H. J. Hickes (2002), He diffusion and (U–Th)/He thermochronometry of zircon: initial results from fish canyon tuff and gold butte, *Tectonophysics*, *349*(1-4), 297–308, doi: 10.1016/S0040-1951(02)00058-6.
- Reiners, P. W. (2005), Zircon (U-Th)/He thermochronometry, *Reviews in Mineralogy and Geochemistry*, *58*(1), 151–179, doi: 10.2138/rmg.2005.58.6.
- P. W., Reiners, and M. T. Brandon (2006), thermochronology understand Using to orogenic erosion, Annual review of earth 419-466, and planetary sciences, 34(1), doi: 10.1146/annurev.earth.34.031405.125202.
- Reiners, P. W., T. L. Spell, S. Nicolescu, and K. A. Zanetti (2004), Zircon (U-Th)/He thermochronometry: He diffusion and comparisons with 40Ar/39Ar dating, *Geochimica et cosmochimica acta*, *68*(8), 1857–1887, doi: 10.1016/j.gca.2003.10.021.
- Replumaz, A., A. M. Negredo, A. Villaseñor, and S. Guillot (2010), Indian continental subduction and slab break-off during tertiary collision, *Terra nova*, pp. no-no, doi:

10.1111/j.1365-3121.2010.00945.x.

- Reynolds, A. (2023), Kinematic evolution of the tangra yumco rift, South-Central tibet: Supplementary data tables, doi: 10.5281/zenodo.10003842.
- Sanchez, V. I., M. Murphy, A. C. Robinson, T. Lapen, and M. Heizler (2013), Tectonic evolution of the India–Asia suture zone since middle eocene time, lopukangri area, south-central tibet, *Journal of Asian Earth Sciences*, *62*, 205–220, doi: 10.1016/J.JSEAES.2012.09.004.
- Schärer, U., R.-H. Xu, and C. J. Allègre (1984), UPb geochronology of gangdese (transhimalaya) plutonism in the Lhasa-Xigaze region, tibet, *Earth and planetary science letters*, *69*(2), 311–320, doi: 10.1016/0012-821x(84)90190-0.
- Schmitz, M. D., and S. A. Bowring (2001), U-Pb zircon and titanite systematics of the fish canyon tuff: an assessment of high-precision U-Pb geochronology and its application to young volcanic rocks, *Geochimica et cosmochimica acta*, 65(15), 2571–2587, doi: 10.1016/s0016-7037(01)00616-0.
- Schmitz, M. D., S. A. Bowring, and T. R. Ireland (2003), Evaluation of duluth complex anorthositic series (AS3) zircon as a U-Pb geochronological standard: new high-precision isotope dilution thermal ionization mass spectrometry results, *Geochimica et cosmochimica acta*, 67(19), 3665–3672, doi: 10.1016/s0016-7037(03)00200-x.
- Shen, T., G. Wang, A. Replumaz, L. Husson, A. A. G. Webb, M. Bernet, P. H. Leloup, P. Zhang, G. Mahéo, and K. Zhang (2020), Miocene subsidence and surface uplift of southernmost tibet induced by indian subduction dynamics, *Geochemistry, Geophysics, Geosystems*, *21*(10), doi: 10.1029/2020gc009078.
- Sheng, Y., S. Jin, M. Comeau, H. Dong, L. Zhang, L. Lei, B. Li, W. Wei, G. Ye, and Z. Lu (2021), Lithospheric structure near the northern Xainza-Dinggye rift, tibetan plateau-implications for rheology and tectonic dynamics, *Journal of Geophysical Research*, *[Solid Earth]*, 126(8), e2020JB021,442, doi: 10.1029/2020JB021442.
- Sobel, E. R., and M. R. Strecker (2003), Uplift, exhumation and precipitation: tectonic and climatic control of late cenozoic landscape evolution in the northern sierras pampeanas, argentina, *Basin Research*, *15*(4), 431–451, doi: 10.1046/j.1365-2117.2003.00214.x.
- Stockli, D. F., M. Taylor, A. Yin, T. M. Harrison, J. D'Andrea, P. Kapp, and L. Ding (2002), Late Miocene-Pliocene inception of EW extension in tibet as evidenced by apatite (U-Th)/He data, in *Geological Society of America Abstracts with Programs*, vol. 34, p. 411.
- Styron, R., M. Taylor, and K. Okoronkwo (2010), Database of active structures from the Indo-Asian collision, *Eos*, *91*(20), 181–182, doi: 10.1029/2010eo200001.
- Styron, R., M. Taylor, K. Sundell, D. Stockli, J. Oalmann, A. Möller, A. T. McCallister, D. Liu, and L. Ding (2013), Miocene initiation and acceleration of extension in the south lunggar rift, western tibet: Evolution of an active detachment system from structural mapping and (U-Th)/He thermochronology, *Tectonics*, *32*(4), 880–907, doi: 10.1002/tect.20053.
- Styron, R., M. Taylor, and K. Sundell (2015), Accelerated extension of tibet linked to the northward underthrusting of indian crust, *Nature geoscience*, 8(2), 131–134, doi: 10.1038/ngeo2336.
- Styron, R. H., M. H. Taylor, and M. A. Murphy (2011), Oblique convergence, arc-parallel extension, and the

- role of strike-slip faulting in the high himalaya, *Geosphere*, 7(2), 582–596, doi: 10.1130/ges00606.1.
- Sundell, K., G. Gehrels, D. Quinn, M. Pecha, D. Giesler, M. Pepper, S. George, and A. White (2020), Agecalcml: An open-source matlab-based data reduction platform for la-icp-ms geochronology and geochemistry data from the arizona laserchron center, in *Geological Society of America Abstracts*, Geological Society of America, doi: 10.1130/abs/2020AM-358944.
- Sundell, K., A. Laskowski, P. Kapp, M. Ducea, and J. Chapman (2021), Jurassic to neogene quantitative crustal thickness estimates in southern tibet, *GSA today: a publication of the Geological Society of America*, *31*(6), 4–10, doi: 10.1130/gsatg461a.1.
- Sundell, K. E., M. H. Taylor, R. H. Styron, D. F. Stockli, P. Kapp, C. Hager, D. Liu, and L. Ding (2013), Evidence for constriction and pliocene acceleration of east-west extension in the north lunggar rift region of west central tibet, *Tectonics*, 32(5), 1454–1479, doi: 10.1002/tect.20086.
- Taylor, M., and A. Yin (2009), Active structures of the Himalayan-Tibetan orogen and their relationships to earthquake distribution, contemporary strain field, and cenozoic volcanism, *Geosphere*, *5*(3), 199–214, doi: 10.1130/ges00217.1.
- Taylor, M., A. Yin, F. J. Ryerson, P. Kapp, and L. Ding (2003), Conjugate strike-slip faulting along the Bangong-Nujiang suture zone accommodates coeval east-west extension and north-south shortening in the interior of the tibetan plateau, *Tectonics*, 22(4), doi: 10.1029/2002tc001361.
- Taylor, M., A. Forte, A. Laskowski, and L. Ding (2021), Active uplift of southern tibet revealed, *GSA today: a publication of the Geological Society of America*, *31*(8), 4–10, doi: 10.1130/gsatg487a.1.
- Thiede, R. C., J. R. Arrowsmith, B. Bookhagen, M. McWilliams, E. R. Sobel, and M. R. Strecker (2006), Dome formation and extension in the tethyan himalaya, leo pargil, northwest india, *Geological Society of America bulletin*, 118(5-6), 635–650, doi: 10.1130/b25872.1.
- Tilmann, F., J. Ni, and INDEPTH III Seismic Team (2003), Seismic imaging of the downwelling indian lithosphere beneath central tibet, *Science*, *300*(5624), 1424–1427, doi: 10.1126/science.1082777.
- Tremblay, M. M., M. Fox, J. L. Schmidt, and others (2015), Erosion in southern tibet shut down at □ 10 ma due to enhanced rock uplift within the himalaya, *Proceedings of the*, *112*(39), 12,030–12,035.
- Turner, S., C. Hawkesworth, J. Liu, N. Rogers, S. Kelley, and P. van Calsteren (1993), Timing of tibetan uplift constrained by analysis of volcanic rocks, *Nature*, *364*(6432), 50–54, doi: 10.1038/364050a0.
- Vermeesch, P. (2018), IsoplotR: A free and open toolbox for geochronology, *Geoscience frontiers*, *9*(5), 1479–1493, doi: 10.1016/J.GSF.2018.04.001.
- Vermeesch, P., and Y. Tian (2014), Thermal history modelling: HeFTy vs. QTQt, *Earth-science reviews*, *139*, 279–290, doi: 10.1016/j.earscirev.2014.09.010.
- Walker, J., B. Tikoff, J. Newman, R. Clark, J. Ash, J. Good, E. G. Bunse, A. Möller, M. Kahn, R. T. Williams, Z. Michels, J. Andrew, and C. Rufledt (2019), StraboSpot data system for structural geology, *Geosphere*, 15(2), 533–547, doi: 10.1130/GES02039.1.
- Wang, C., X. Li, Z. Liu, Y. Li, L. Jansa, J. Dai, and Y. Wei (2012), Revision of the Cretaceous–Paleogene stratigraphic

- framework, facies architecture and provenance of the xigaze forearc basin along the yarlung zangbo suture zone, *Gondwana Research*, *22*(2), 415–433, doi: 10.1016/J.GR.2011.09.014.
- Wang, C., L. Ding, F.-L. Cai, H.-Q. Wang, L.-Y. Zhang, and Y.-H. Yue (2022), Evolution of the sumdo paleo-tethyan ocean: Constraints from permian luobadui formation in lhasa terrane, south tibet, *Palaeogeography, palaeoclimatology, palaeoecology, 595*(110974), 110,974, doi: 10.1016/j.palaeo.2022.110974.
- Wang, E., P. J. J. Kamp, G. Xu, K. V. Hodges, K. Meng, L. Chen, G. Wang, and H. Luo (2015), Flexural bending of southern tibet in a retro foreland setting, *Scientific reports*, *5*(1), 12,076, doi: 10.1038/srep12076.
- Wang, H., J. R. Elliott, T. J. Craig, T. J. Wright, J. Liu-Zeng, and A. Hooper (2014), Normal faulting sequence in the Pumqu-Xainza rift constrained by InSAR and teleseismic body-wave seismology, *Geochemistry*, *Geophysics*, *Geosystems*, 15(7), 2947–2963, doi: 10.1002/2014gc005369.
- Wang, J., X. Hu, F.-Y. Wu, and L. Jansa (2010), Provenance of the liuqu conglomerate in southern tibet: A paleogene erosional record of the Himalayan–Tibetan orogen, *Sedimentary geology*, *231*(3-4), 74–84, doi: 10.1016/J.SEDGEO.2010.09.004.
- Wang, J., X. Hu, E. Garzanti, and F.-Y. Wu (2013), Upper oligocene-lower miocene gangrinboche conglomerate in the xigaze area, southern tibet: Implications for himalayan uplift and Paleo-Yarlung-Zangbo initiation, *The Journal of geology*, 121(4), 425–444, doi: 10.1086/670722.
- Wells, M. L., and T. D. Hoisch (2008), The role of mantle delamination in widespread late cretaceous extension and magmatism in the cordilleran orogen, western united states, *Geological Society of America bulletin*, 120(5-6), 515–530, doi: 10.1130/b26006.1.
- Wells, M. L., T. D. Hoisch, A. M. Cruz-Uribe, and J. D. Vervoort (2012), Geodynamics of synconvergent extension and tectonic mode switching: Constraints from the Sevier-Laramide orogen, *Tectonics*, *31*(1), doi: 10.1029/2011TC002913.
- Wemicke, B. (1992), Cenozoic extensional tectonics of the US cordillera, *The Geology of North America*, *3*, 553–582.
- Whipp, D. M., D. A. Kellett, I. Coutand, and R. A. Ketcham (2022), Short communication: Modeling competing effects of cooling rate, grain size, and radiation damage in low-temperature thermochronometers, *Geochronology*, *4*(1), 143–152, doi: 10.5194/gchron-4-143-2022.
- Willett, S. D., S. W. McCoy, J. T. Perron, L. Goren, and C.-Y. Chen (2014), Dynamic reorganization of river basins, *Science*, *343*(6175), 1248,765, doi: 10.1126/science.1248765.
- Williams, H., S. Turner, S. Kelley, and N. Harris (2001), Age and composition of dikes in southern tibet: New constraints on the timing of east-west extension and its relationship to postcollisional volcanism, *Geology*, *29*(4), 339, doi: 10.1130/0091-7613(2001)029<0339:aacodi>2.0.co;2.
- Williams, H., S. Turner, J. Pearce, S. Kelley, and N. Harris (2004), Nature of the source regions for post-collisional, potassic magmatism in southern and northern tibet from geochemical variations and inverse trace element modelling, *Journal of Petrology*, 45(3), 555–607, doi:

10.1093/PETROLOGY/EGG094.

- Wolff, R., R. Hetzel, I. Dunkl, Q. Xu, M. Bröcker, and A. Anczkiewicz (2019), High-angle normal faulting at the tangra yumco graben (southern tibet) since □15 ma, *The Journal of geology*, *127*(1), 15–36, doi: 10.1086/700406.
- Wolff, R., R. Hetzel, K. Hölzer, I. Dunkl, Q. Xu, A. A. Anczkiewicz, and Z. Li (2023), Rift propagation in south tibet controlled by under-thrusting of india: a case study of the tangra yumco graben (south tibet), *Journal of the Geological Society*, *180*(2), jgs2022–090, doi: 10.1144/jgs2022-090.
- Wu, C., K. D. Nelson, G. Wortman, S. D. Samson, Y. Yue, J. Li, W. S. F. Kidd, and M. A. Edwards (1998), Yadong cross structure and south tibetan detachment in the east central himalaya (89–90 e), *Tectonics*, *17*(1), 28–45.
- Wu, F.-Y., W. Ji, C.-Z. Liu, and S. Chung (2010), Detrital zircon U–Pb and hf isotopic data from the xigaze fore-arc basin: Constraints on transhimalayan magmatic evolution in southern tibet, *Chemical geology*, *271*(1-2), 13–25, doi: 10.1016/J.CHEMGEO.2009.12.007.
- Wu, H., C. Li, M.-J. Xu, and X. Li (2015), Early cretaceous adakitic magmatism in the dachagou area, northern lhasa terrane, tibet: Implications for slab roll-back and subsequent slab break-off of the lithosphere of the Bangong-Nujiang ocean, *Journal of Asian Earth Sciences*, 97, 51–66, doi: 10.1016/J.JSEAES.2014.10.014.
- Wu, H. R., D. A. Wang, L. C. Wang, and Others (1977), Cretaceous in Lhaze–Gyangze, southern xizang, Scientia Geologica Sinica, 3(250), e261.
- Yin, A. (2000), Mode of cenozoic east-west extension in tibet suggesting a common origin of rifts in asia during the Indo-Asian collision, *Journal of geophysical research*, 105(B9), 21,745–21,759, doi: 10.1029/2000jb900168.
- Yin, A. (2006), Cenozoic tectonic evolution of the himalayan orogen as constrained by along-strike variation of structural geometry, exhumation history, and foreland sedimentation, *Earth-science reviews*, *76*(1-2), 1–131, doi: 10.1016/j.earscirev.2005.05.004.
- Yin, A., and T. M. Harrison (2000), Geologic evolution of the Himalayan-Tibetan orogen, *Annual review of earth and planetary sciences*, *28*(1), 211–280, doi: 10.1146/annurev.earth.28.1.211.
- Yin, A., and M. H. Taylor (2011), Mechanics of v-shaped conjugate strike-slip faults and the corresponding continuum mode of continental deformation, *Geological Society of America bulletin*, *123*(9-10), 1798–1821, doi: 10.1130/b30159.1.
- Yin, A., T. M. Harrison, F. J. Ryerson, C. Wenji, W. S. F. Kidd, and P. Copeland (1994), Tertiary structural evolution of the gangdese thrust system, southeastern tibet, *Journal of geophysical research*, *99*(B9), 18,175–18,201, doi: 10.1029/94jb00504.
- Yin, A., T. M. Harrison, M. A. Murphy, M. Grove, S. Nie, F. J. Ryerson, W. Xiao Feng, and C. Zeng Le (1999a), Tertiary deformation history of southeastern and southwestern tibet during the Indo-Asian collision, *Geological Society of America bulletin*, 111(11), 1644, doi: 10.1130/0016-7606(1999)111<1644:tdhosa>2.3.co;2.
- Yin, A., P. A. Kapp, M. A. Murphy, C. E. Manning, T. Mark Harrison, M. Grove, D. Lin, D. Xi-Guang, and W. Cun-Ming (1999b), Significant late neogene east-west extension in northern tibet, *Geology*, 27(9), 787, doi: 10.1130/0091-7613(1999)027<0787:slnewe>2.3.co;2.
- Zhang, J., and L. Guo (2007), Structure and geochronology

- of the southern Xainza-Dinggye rift and its relationship to the south tibetan detachment system, Journal of Asian Earth Sciences, 29(5-6), 722-736, doi: 10.1016/j.jseaes.2006.05.003.
- Zhang, J., L. Guo, and L. Ding (2002), Structural characteristics of middle and southern Xainza-Dinggye normal fault system and its relationship to southern tibetan detachment system, Chinese science bulletin = *Kexue tongbao*, *47*, 1063–1069, doi: 10.1360/02TB9239.
- Zhang, J., J. Dai, X. Qian, Y. Ge, and C. Wang (2017), Sedimentology, provenance and geochronology of the miocene qiuwu formation: Implication for the uplift history of southern tibet, Geoscience frontiers, 8(4), 823-839, doi: 10.1016/j.gsf.2016.05.010.
- Zhang, L., M. Ducea, L. Ding, A. Pullen, P. Kapp, and D. Hoffman (2014), Southern tibetan Oligocene-Miocene adakites: A record of indian slab tearing, Lithos, 210, 209-223, doi: 10.1016/J.LITHOS.2014.09.029.
- Zhang, P.-Z., Z. Shen, M. Wang, W. Gan, R. Bürgmann, P. Molnar, Q. Wang, Z. Niu, J. Sun, J. Wu, and Others (2004), Continuous deformation of the tibetan plateau from global positioning system data, Geology, 32(9), 809-812.
- Zhang, Y., F. Huang, J. Xu, Y. Zeng, B. Wang, M. Lv, L. Zhang, M. Li, Z. Zhang, Y. Tian, Q. Liu, and

- L. Zhang (2022), Origin of the volcanic rocks in dianzhong formation, central lhasa terrane, tibet: implication for the genesis of syn-collisional magmatism and Neo-Tethyan slab roll-back, Soviet economy, 65(1), 21-39, doi: 10.1080/00206814.2022.2031314.
- Zhu, B., W. S. F. Kidd, D. B. Rowley, B. S. Currie, and N. Shafique (2005), Age of initiation of the India-Asia collision in the East-Central himalaya, The Journal of geology, 113(3), 265-285, doi: 10.1086/428805.
- Zhu, D.-C., Z.-D. Zhao, Y. Niu, X.-X. Mo, S.-L. Chung, Z.-Q. Hou, L.-Q. Wang, and F.-Y. Wu (2011), The Ihasa terrane: Record of a microcontinent and its histories of drift and growth, Earth and planetary science letters, 301(1), 241–255, doi: 10.1016/j.epsl.2010.11.005.
- Zhu, D.-C., Z.-D. Zhao, Y. Niu, Y. Dilek, Q. Wang, W.-H. Ji, G.-C. Dong, Q.-L. Sui, Y.-S. Liu, H.-L. Yuan, and Others (2012), Cambrian bimodal volcanism in the lhasa terrane, southern tibet: record of an early paleozoic andean-type magmatic arc in the australian proto-tethyan margin, Chemical geology, 328, 290-308.
- Zhu, D.-C., Q. Wang, Z.-D. Zhao, S.-L. Chung, P. A. Cawood, Y. Niu, S.-A. Liu, F.-Y. Wu, and X.-X. Mo (2015), Corrigendum: Magmatic record of India-Asia collision, Scientific reports, 5(1), 17,236, doi: 10.1038/srep17236.